Mon. Not. R. Astron. Soc. **000**, 1–?? (0000) Printed 13 March 2017 (MN LATEX style file v2.2)

A powerful flare from Sgr A* confirms the synchrotron nature of the X-ray emission

G. Ponti[1⋆], E. George[1], S. Scaringi[1,2], S. Zhang[3,4], C. Jin[1], J. Dexter[1], R. Terrier[5,6], M. Clavel[7], N. Degenaar[8,9], F. Eisenhauer[1], R. Genzel[1], S. Gillessen[1], A. Goldwurm[5,6], M. Habibi[1], D. Haggard[10,11], C. Hailey[2], F. Harrison[12], A. Merloni[1], K. Mori[2], K. Nandra[1], T. Ott[1] O. Pfuhl[1], P. M. Plewa[1], and I. Waisberg[1]

[1] *Max Planck Institute fur Extraterrestriche Physik, 85748, Garching, Germany*
[2] *Department of Physics and Astronomy, University of Canterbury, Private Bag 4800 Christchurch, New Zealand*
[3] *Columbia Astrophysics Laboratory, Columbia University, New York, NY 10027, USA*
[4] *MIT Kavli Institute for Astrophysics and Space Research*
[5] *Unité mixte de recherche Astroparticule et Cosmologie, 10 rue Alice Domon et Léonie Duquet, 75205 Paris, France*
[6] *Service d'Astrophysique (SAp), IRFU/DRF/CEA-Saclay, 91191 Gif-sur-Yvette Cedex, France*
[7] *Space Sciences Laboratory, 7 Gauss Way, University of California, Berkeley, CA 94720-7450, USA*
[8] *Institute of Astronomy, University of Cambridge, Madingley Road, Cambridge CB3 OHA, UK*
[9] *Anton Pannekoek Institute for Astronomy, University of Amsterdam, Science Park 904, 1098 XH, Amsterdam, the Netherlands*
[10] *McGill University, Department of Physics, 3600 rue University, Montréal, QC, H3A 2T8*
[11] *McGill Space Institute, 3550 rue University, Montréal, QC, H3A 2A7 McGill*
[12] *Jet Propulsion Laboratory, California Institute of Technology, 4800 Oak Grove Drive, Mail Stop 169-221, Pasadena, CA 91109, USA*

13 March 2017

ABSTRACT

We present the first fully simultaneous fits to the NIR and X-ray spectral slope (and its evolution) during a very bright flare from Sgr A*, the supermassive black hole at the Milky Way's center. Our study arises from ambitious multi-wavelength monitoring campaigns with *XMM-Newton*, *NuSTAR* and *SINFONI*. The average multi-wavelength spectrum is well reproduced by a broken power-law with $\Gamma_{NIR} = 1.7 \pm 0.1$ and $\Gamma_X = 2.27 \pm 0.12$. The difference in spectral slopes ($\Delta\Gamma = 0.57 \pm 0.09$) strongly supports synchrotron emission with a cooling break. The flare starts first in the NIR with a flat and bright NIR spectrum, while X-ray radiation is detected only after about 10^3 s, when a very steep X-ray spectrum ($\Delta\Gamma = 1.8 \pm 0.4$) is observed. These measurements are consistent with synchrotron emission with a cooling break and they suggest that the high energy cut-off in the electron distribution (γ_{max}) induces an initial cut-off in the optical-UV band that evolves slowly into the X-ray band. The temporal and spectral evolution observed in all bright X-ray flares are also in line with a slow evolution of γ_{max}. We also observe hints for a variation of the cooling break that might be induced by an evolution of the magnetic field (from $B \sim 30 \pm 8$ G to $B \sim 4.8 \pm 1.7$ G at the X-ray peak). Such drop of the magnetic field at the flare peak would be expected if the acceleration mechanism is tapping energy from the magnetic field, such as in magnetic reconnection. We conclude that synchrotron emission with a cooling break is a viable process for Sgr A*'s flaring emission.

Key words: Galaxy: centre; X-rays: Sgr A*; black hole physics; methods: data analysis; stars: black holes;

1 INTRODUCTION

Sgr A*, the supermassive black hole (BH) at the Milky Way's center, with a bolometric luminosity of $L \sim 10^{36}$ erg s^{-1} is currently characterised by an exceptionally low Eddington ratio ($\sim 10^{-8}$; Genzel et al. 2010a), despite indications that Sgr A* might have been brighter in the past (see Ponti et al. 2013 for a review). Therefore, Sgr A* provides us with the best chance to get a glimpse of the physical processes at work in quiescent BH.

Sgr A* has been intensively studied over the past several

⋆ ponti@mpe.mpg.de

decades at various wavelengths. The black points (upper-lower limits) in Fig. 1 show a compilation of measurements of Sgr A*'s quiescent emission from radio to mid-IR (values are taken from Falcke et al. 1998; Markoff et al. 2001; An et al. 2005; Marrone et al. 2006; Schödel et al. 2007; 2011; Dodds-Eden et al. 2009; Bower et al. 2015; Brinkerink et al. 2015; Liu et al. 2016; Stone et al. 2016) as well as the radiatively inefficient accretion flow model proposed by Yuan et al. (2003). The bulk of Sgr A*'s steady radiation is emitted at sub-mm frequencies, forming the so called "sub-mm bump" (dot-dashed line in Fig. 1). This emission is linearly polarised (2-9 %; Marrone et al. 2006; 2007), slowly variable and decreases rapidly with frequency (with stringent upper limits in the mid-IR band; Schödel et al. 2007; Trap et al. 2011). This indicates that the sub-mm radiation is primarily due to optically thick synchrotron radiation originating in the central $\sim 10\ R_S$[1] and produced by relativistic ($\gamma_e \sim 10$, where γ_e is the electron Lorentz factor) thermal electrons with temperature and densities of $T_e \sim$ few $10^{10}\ K$ and $n_e \sim 10^6$ cm^{-3}, embedded in a magnetic field with a strength of $\sim 10 - 50$ G (Loeb & Waxman 2007; Genzel et al. 2010a; in Fig. 1 a possible inverse Compton component is also shown). Moreover, Faraday rotation measurements constraint the accretion rate at those scales to be within 2×10^{-9} and 2×10^{-7} M$_\odot$ yr^{-1} (Marrone et al. 2006; 2007; Genzel et al. 2010a).

At low frequency ($\nu < 10^{11}$ Hz) Sgr A*'s SED changes slope ($F_\nu \propto \nu^{0.2}$) showing excess emission above the extrapolation of the thermal synchrotron radiation and variability on time-scales of hours to years (Falcke et al. 1998; Zhao et al. 2003; 2004; Herrnstein et al. 2004). This suggests either the presence of a non-thermal tail in the electron population, taking ~ 1 % of the steady state electron energy (Özel et al. 2000; see dashed line in Fig. 1) or a compact radio jet (Falcke et al. 1998; Mościbrodzka et al. 2009; 2013; 2014). The presence of this non-thermal tail is well constrained at low radio frequencies, while its extrapolation in the mid and near infra-red band is rather uncertain (see dashed line in Fig. 1).

Sgr A* also appears as a faint ($L_{2-10\ keV} \sim 2 \times 10^{33}$ erg s^{-1}) X-ray source (Baganoff et al. 2003; Xu et al. 2006) observed to be extended with a size of about $\sim 1''$. The observed size is comparable to the Bondi radius and the quiescent X-ray emission is thought to be the consequence of material that is captured at a rate of 10^{-6} M$_\odot$ yr^{-1} from the wind of nearby stars (Melia 1992; Quataert 2002; Cuadra et al. 2005; 2006; 2008). Indeed, this emission is thought to be produced via bremsstrahlung emission from a hot plasma with $T \sim 7 \times 10^7$ K, density $n_e \sim 100$ cm^{-3} emitted from a region $\sim 10^5$ R$_S$ (Quataert 2002; see dotted line in Fig. 1).

For more than a decade it has been known that Sgr A* also shows flaring activity both in X-rays and IR (Baganoff et al. 2001; Goldwurm et al. 2003; Genzel et al. 2003; Ghez et al. 2004; Porquet et al. 2003; 2008; Bélanger et al. 2005; Eckart et al. 2004; 2006; Marrone et al. 2008; Nowak et al. 2012; Haubois et al. 2012; Neilsen et al. 2013; 2015; Degenaar et al. 2013; Barrière et al. 2014; Moussoux et al. 2015; Ponti et al. 2015a; Yuan & Wang 2016). X-ray flares appear as clear enhancements above the constant quiescent emission, with peak luminosities occasionally exceeding the quiescent luminosity by up to two orders of magnitude (see the blue points in Fig. 1 for an example of a very bright flare; Baganoff et al. 2001; Porquet et al. 2003; 2008; Nowak et al. 2012). X-ray flare durations, fluences, and peak luminosities are correlated (Neilsen et al. 2013). Moreover, weak X-ray flares are more common than strong ones (Neilsen et al. 2013; Ponti et al. 2015a). The appearance of the X-ray light curves suggests that flares are individual and distinct events, randomly punctuating an otherwise quiescent source (Neilsen et al. 2013; Ponti et al. 2015a).

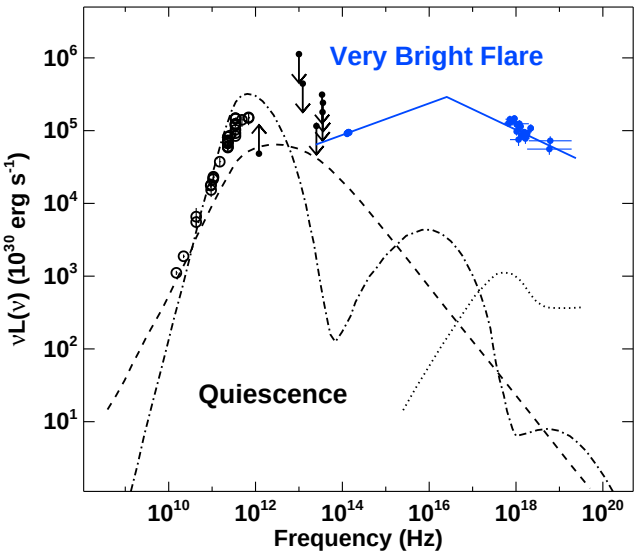

Figure 1. Multi-wavelength emission from Sgr A*. The radio to mid-IR data points (open circles as well as upper-lower limits) constrain Sgr A*'s quiescent emission (these constraints are taken from the literature, see text). The black lines show the radiatively inefficient accretion disc model proposed by Yuan et al. (2003). The dash-dotted black line shows the contribution from the thermal electrons with $T_e \sim few\ 10^{10}\ K$ and $n_e \sim 10^6$ cm^{-3}, embedded in a magnetic field with strength of $\sim 10-50$ G producing the sub-mm peak and (possibly) inverse Compton emission at higher energies. The dashed line shows the contribution from a non-thermal tail in the electron population, while the dotted line shows the bremsstrahlung emission from hot plasma at the Bondi radius (Quataert 2002). The blue filled data points shows the mean NIR and X-ray spectra of the very bright flare VB3 and the blue solid line shows the best fit power-law with cooling break (see also Fig. 6).

Typically X-ray flares coincide with clear peaks in the near infrared (NIR) light curves (e.g. Genzel et al. 2003; Clenet et al. 2004; Ghez et al. 2004; Eckart et al. 2006; 2008; Meyer et al. 2006; 2007; 2008; Yusef-Zadeh et al. 2006; 2009; Hornstein et al. 2007; Do et al. 2009). However, the appearance of the NIR light curves is significantly different from the X-ray ones. Indeed, the NIR and sub-mm emission of Sgr A* are continuously varying and they can be described by a red noise process at high frequencies, breaking at time-scales longer than a fraction of a day[2] (Do et al. 2009; Meyer et al. 2009; Dodds-Eden et al. 2011; Witzel et al. 2012; Dexter et al. 2014; Hora et al. 2014). Therefore, the NIR light curves do not support the notion of flares as individual events; they would alternatively corroborate the concept that flares are simply peaks of emission on a continuous red noise process. Despite the fact that the notion of NIR-flares is still unsettled, *we will refer to the X-ray flares, and by extension, to the NIR peaks in emission, as flares throughout this paper*.

The origin and radiative mechanism of the flares of Sgr A* are still not completely understood. Several multi-wavelength cam-

[1] R_S is the Schwarzschild radius $R_S = 2GM_{BH}/c^2$, where M_{BH} is the BH mass, G the gravitational constant and c the speed of light.

[2] Interestingly, AGN of similar BH mass, but clearly much higher accretion rate, show power density spectra (PDS) of their X-ray light curves consistent with the NIR PDS of Sgr A* (Meyer et al. 2009).

paigns have been performed, but the radiative mechanisms at work during the flares is still highly debated (Eckart et al. 2004, 2006, 2008, 2009, 2012; Yusef-Zadeh et al. 2006, 2008, 2009; Hornstein et al. 2007; Marrone et al. 2008; Dodds-Eden et al. 2009; Trap et al. 2011; Barriere et al. 2014). Indeed, even though 15 years have passed since the launch of *XMM-Newton* and *Chandra*, simultaneous X-ray and NIR spectra of a bright flare (as these allow a precise determination of the spectral index in the two bands) has not yet been published[3].

Polarisation in the sub-mm and NIR bands suggests that the NIR radiation is produced by synchrotron emission. The origin of the X-ray emission is still debated. Indeed, the X-ray radiation could be produced by synchrotron itself or inverse Compton processes such as synchrotron self-Compton or external Compton (see Genzel et al. 2010a for a review). Different models explain the data with a large range of physical parameters, however, models with synchrotron emission extending with a break from NIR to the X-ray seem to be best able to account for the X-ray data with reasonable physical parameters (Dodds-Eden et al. 2009; Trap et al. 2010; Dibi et al. 2014; 2016; Barriere et al. 2014).

We report here the first simultaneous observation of the X-ray (*XMM-Newton*), hard X-ray (*NuSTAR*), and NIR (*SINFONI*) spectra of a very bright flare of Sgr A*, which occurred between 2014 August 30^{th} and 31^{st} (Ponti et al. 2015a; 2015c), and an analysis of flare models which could explain the emission. The remainder of this paper is organised as follows: Section 2 details the reduction of the X-ray and NIR data. In section 3 we present a characterisation of the obscuration and mean spectral properties of the very bright flares observed by *XMM-Newton*. In section 4 we investigate the mean properties of the VB3 flare, in particular we constrain the radiative mechanism through the study of the mean multi-wavelength spectrum. In section 5, we follow the evolution of the flare emission to determine time-dependent parameters of the emission models. Section 6 scrutinises a "quiescent" interval after the very bright flare. In Section 7 we focus the analysis on the X-ray band only and we study the evolution of the X-ray spectral shape throughout all bright and very bright X-ray flares. We discuss the results of the model fits in section 8 and conclude in section 9.

2 DATA REDUCTION

We consider two sets of data in this paper. The first set comprises simultaneous X-ray (*XMM-Newton* and *NuSTAR*) and NIR data of one very bright flare, called VB3 (see Ponti et al. 2015 for the definition of the naming scheme). The analyses of the *XMM-Newton*, *NuSTAR* and *SINFONI* data on flare VB3 are discussed in sections 2.2, 2.3 and 2.4. The second set of data consists of all of Sgr A*'s bright or very bright X-ray flares as detected with *XMM-Newton*. The reduction of this set of data is discussed in section 2.2 along with the description of the flare VB3.

2.1 Basic assumptions

Throughout the paper we assume a distance to Sgr A* of 8.2 kpc and a mass of M$= 4.4 \times 10^6$ M$_\odot$ (Genzel et al. 2010a). The errors and upper limits quoted on spectral fit results correspond to 90 % confidence level for the derived parameters (unless otherwise specified), while uncertainties associated with measurements reported in plots are displayed at the 1 σ confidence level. The neutral absorption affecting the X-ray spectra is fitted with the model TBNEW[4] (see Wilms et al. 2000) with the cross sections of Verner et al. (1996) and abundances of Wilms et al. (2000). The dust scattering halo is fitted with the model FGCDUST in XSPEC (Jin et al. 2016; see §3) and it is assumed to be the same as the "foreground" component along the line of sight towards AX J1745.6-2901 (Jin et al. 2016). More details on the implications of this assumptions are included in §3 and Appendix B. In §3 we justify the assumption of a column density of neutral absorbing material of $N_H = 1.60 \times 10^{23}$ cm^{-2} and we apply it consistently thereafter. Throughout our discussion we assume that the effects of beaming are negligible, as well as a single zone emitting model for the source.

Unless otherwise stated, we follow Dodds-Eden et al. (2009) and we assume a constant escape time of the synchrotron emitting electrons equal to $t_{esc} = 300$ s. Under this assumption, the frequency of the synchrotron cooling break can be used to derive the amplitude of the source magnetic field.

2.2 *XMM-Newton*

In this work, we considered all of the *XMM-Newton* observations during which either a bright or very bright flare has been detected through the Bayesian block analysis performed by Ponti et al. (2015a). Full details about the observation identification (obsID) are reported in Tab. 1.

Starting from the *XMM-Newton* observation data files, we reprocessed all of the data sets with the latest version (15.0.0) of the *XMM-Newton* Science Analysis System (SAS), applying the most recent (as of 2016 April 27, valid for the observing day) calibrations. Whenever present, we eliminated strong soft proton background flares, typically occurring at the start or end of an observation, by cutting the exposure time as done in Ponti et al. (2015a; see Tab. 7). To compare data taken from different satellites and from the ground, we performed barycentric correction by applying the BARYCEN task of SAS. The errors quoted on the analysis of the light curves correspond to the 1 σ confidence level (unless otherwise specified). XSPEC v12.8.2 and MATLAB are used for the spectral analysis and the determination of the uncertainties on the model parameters.

We extracted the source photons from a circular region with $10''$ radius, corresponding to $\sim 5.1 \times 10^4$ AU, or $\sim 6.5 \times 10^5$ R_S (Goldwurm et al. 2003; Bélanger et al. 2005; Porquet et al. 2008; Trap et al. 2011; Mossoux et al. 2015). For each flare we extracted source photons during the time window defined by the Bayesian block routine (applied on the EPIC-pn light curve, such as in Ponti et al. 2015a), adding 200 s before and after the flare (see Tab. 1). Background photons have been extracted from the same source regions by selecting only quiescent periods. The latter are defined as moments during which no flare of Sgr A* is detected by the Bayesian block procedure (Ponti et al. 2015a) and additionally leaving a 2 ks gap before the start and after the end of each flare.

Given that all of the observations were taken in Full frame mode, pile-up is expected to be an issue only when the count rate

[3] Indeed, the few multi-wavelength campaigns that caught a very bright X-ray flare were missing spectroscopic information in the NIR band (e.g., Dodds-Eden et al. 2009), while the few campaigns with spectroscopic information in both bands, failed to detect a bright X-ray flare with a NIR counterpart (e.g., flare A and B of Trap et al. 2011).

[4] http://pulsar.sternwarte.uni-erlangen.de/wilms/research/tbabs/

XMM-Newton obsID	Date	t_{start} TT_{TBD}	t_{stop} TT_{TBD}	NAME
Archival data				
0111350301	2002-10-03	150026757	150029675	**VB1**
		150026757	150027730	VB1-Rise
		150027730	150028702	VB1-Peak
		150028702	150029675	VB1-Dec
0402430401	2007-04-04	292050970	292054635	**VB2**
		292050970	292052192	VB2-Rise
		292052192	292053413	VB2-Peak
		292053413	292054635	VB2-Dec
		292084140	292087981	**B1**
0604300701	2011-03-30	417894177	417896560	**B2**
This campaign				
0743630201	2014-08-30	525829293	525832367	**VB3**
		525827793	525829193	VB3-Pre
		525829193	525830593	VB3-Rise
		525830593	525831843	VB3-Peak
		525831843	525832743	VB3-Dec
		525832743	525834893	VB3-Post
	2014-08-31	525846661	525848532	**B3**
0743630301	2014-09-01	525919377	525924133	**B4**
0743630501	2014-09-29	528357937	528365793	**B5**

Table 1. List of *XMM-Newton* observations and flares considered in this work. The flares are divided into two categories, bright (B) and very bright (VB), classified according to their total fluence (see Ponti et al. 2015a). The different columns show the *XMM-Newton* obsID, flare start and end times in Terrestrial Time (TT‡; see Appendix A) units and flare name, respectively. The flare start and end times are barycentric corrected (for comparison with multi-wavelength data) and correspond to the flare start time (minus 200 s) and flare stop time (plus 200 s) obtained through a Bayesian block decomposition (Ponti et al 2015a; please note that the time stamps in Ponti et al 2015a are not barycentric corrected). Neither a moderate nor weak flare is detected during these *XMM-Newton* observations. To investigate the presence of any spectral variability within each very bright flare, we extracted three equal duration spectra catching the flare rise, peak and decay, with the exception of VB3. In the latter case, we optimised the duration of these time intervals according to the presence of simultaneous NIR observations (see Fig. 5).

exceeds $\sim$ 2 cts/s[5]. This threshold is above the peak count rate registered even during the brightest flares of Sgr A*. This provides *XMM-Newton* with the key advantage of being able to collect pile-up free, and therefore unbiased, spectral information even for the brightest flares.

For each spectrum, the response matrix and effective area have been computed with the XMM-SAS tasks RMFGEN and ARFGEN. See Appendix A for further details on the *XMM-Newton* data reduction.

2.3 *NuSTAR*

To study the flare characteristics in the broad X-ray band, we analyzed the two *NuSTAR* observations (obsID: 30002002002, 30002002004) taken in fall 2014 in coordination with *XMM-Newton*. We processed the data using the *NuSTAR Data Analysis Software NuSTARDAS* v.1.3.1. and HEASOFT v. 6.13, filtered for periods of high instrumental background due to SAA passages and known bad detector pixels. Photon arrival times were corrected for on-board clock drift and precessed to the Solar System barycenter using the JPL-DE200 ephemeris. For each observation, we registered the images with the brightest point sources available in individual observations, improving the astrometry to $\sim 4''$. We made use of the date obtained by both focal plane modules FPMA and FPMB.

Four *XMM-Newton* flares were captured in the coordinated *NuSTAR* observations: VB3, B3, B4 and B5. We extract the *NuSTAR* flare spectra using the same flaring intervals as determined from the *XMM-Newton* data (see Table 1). The flare times are barycentric corrected for comparison between different instruments. Due to interruption caused by earth occultation, *NuSTAR* good time intervals (GTIs) detected only a portion of the flares. For flare VB3, *NuSTAR* captured the first $\sim 1215\ s$ of the full flare, corresponding to pre-, rising- and part of the peak-flare, while the dec- and post-flare intervals were missed. Similarly, part of the rising-flare stage of flare B3 and the middle half of flare B4 were captured in the *NuSTAR* GTIs. Flare B5 was not significantly detected with *NuSTAR*, resulting in $\sim 2\sigma$ detection in the *NuSTAR* energy band.

To derive the flare spectra, we used a source extraction region with $30''$ radius centered on the position of Sgr A*. While the source spectra were extracted from the flaring intervals, the background spectra were extracted from the same region in the off-flare intervals within the same observation. The spectra obtained by FPMA and FPMB are combined and then grouped with a minimum of 3σ signal-to-noise significance per data bin, except the last bin at the high-energy end for which we require a minimum of 2σ significance.

2.4 *SINFONI*

2.4.1 *Observations and data reduction*

We observed Sgr A* with *SINFONI* (Eisenhauer et al. 2003; Bonnet et al. 2004) at VLT between 30-08-2014 23:19:38 UTC and 31-08-2014 01:31:14 UTC. *SINFONI* is an adaptive optics (AO) assisted integral-field spectrometer mounted at the Cassegrain focus of Unit Telescope 4 (Yepun) of the ESO Very Large Telescope. The field of view used for this observation was $0.8'' \times 0.8''$, which is divided into 64×32 spatial pixels by the reconstruction of the pseudoslit into a 3D image cube. We observed in H+K bands with a spectral resolution of ~ 1800.

We accumulated seven spectra (see observation log in Tab. 3) of 600 s each using an object-sky-object observing pattern. There are gaps between observations for the 600 s sky exposures, as well as a longer gap due to a brief telescope failure during what would have been an additional object frame at the peak of the X-ray flare. In total, we accumulated four sky frames on the sky field ($712''$ west, $406''$ north of Sgr A*). During our observations, the seeing was $\sim 0.7''$ and the optical coherence time was $\sim$ 2.5 ms. The AO loop was closed on the closest optical guide star (m_R = 14.65; $10.8''$ east, $18.8''$ north of Sgr A*), yielding a spatial resolution of $\sim$ 90 mas FWHM at 2.2 μm, which is $\sim$1.5 times the diffraction limit of UT4 in K band.

The reduction of the *SINFONI* data followed the standard steps. The object frames were sky subtracted using the nearest-in-time sky frame to correct for instrumental and atmospheric backgrounds. We applied bad pixel correction, flat-fielding, and distortion correction to remove the intrinsic distortion in the spectrograph. We performed an initial wavelength calibration with calibration source arc lamps, and then fine-tuned the wavelength cali-

[5] *XMM-Newton* User Handbook Issue 2.12, Longinotti et al. 2014

Coordinated *NuSTAR* and *XMM-Newton* observations and flares detected				
NuSTAR obsID	t_{start}	Exposure (ks)	Joint *XMM-Newton* obsID	NAME
30002002002	2014-08-30 19:45:07	59.79 ks	0743630201	VB3, B3
			0743630301	B4
30002002004	2014-09-27 17:31:07	67.24 ks	0743630501	B5

Table 2. The different columns show the *NuSTAR* obsID, observation start time, total exposure, coordinated *XMM-Newton* obsID and the flares detected in the observation.

bration using the atmospheric OH lines of the raw frames. Finally, we assembled the data into cubes with a spatial grid of 12.5 mas per pixel.

2.4.2 *Sgr A* spectrum extraction*

The source spectrum extraction uses a procedure to extract a noisy spectrum from Sgr A*. This can then be binned and the scatter within a bin used as an estimate of the error on the flux in that bin. In each of the seven data cubes, we use a rectangular region of the spatial dimensions of size ($0.31'' \times 0.36''$) centered roughly between Sgr A* and the bright star S2 (0.05" south of S2). Within this region are four known S-stars, S2, S17, S19, and S31. Figure 2 shows a combined data cube assembled from the seven observations, as well as a simulated image of the Galactic centre S-stars. The four known stars used in the fitting procedure are labelled in both images. We extract $\sim$100 noisy images from the data cube by collapsing the cube along the spectral direction (median in the spectral direction) in bins with 3.5 nm width (seven spectral channels per bin) in the spectral range 2.03-2.39 μm. This initial binning is necessary, as the signal to noise of a single spectral channel is not high enough on its own to perform the next step.

In each noisy image, we determine the flux of Sgr A* from a fit with 6 Gaussians to the image. Five Gaussians with a common (variable) width describe the five sources in each image. The sixth Gaussian has a width of 3.5 times wider than the sources, and describes the AO seeing halo of the brightest star, S2, which has a K magnitude of $\sim$14. The seeing halos of the dimmer stars (K magnitude $<$15) are neglected in the fit. The positions of the four stars relative to one another and to Sgr A* are fixed based on the known positions of the stars. The flux ratios of the four stars are fixed based on previous photometric measurements of the stars. Note that fixing the flux ratios assumes that the spectral indices of the various S-stars are not significantly different, an excellent assumption given the strong extinction toward the Galactic center (GC).

The final fit has five free parameters: The overall amplitude of the S-stars, the background, the Gaussian width of the sources, the flux ratio of the seeing halo/S2, and the flux ratio of Sgr A*/S2. This fitting procedure allows a measurement of the variability of Sgr A* in the presence of variations (in time and wavelength) in the background, Strehl ratio, and seeing. The result of this procedure is a flux ratio of Sgr A*/S2 in each of the $\sim$ 100 spectral bins.

We obtain a noisy, color-corrected spectrum of Sgr A* by multiplying a calculated spectrum of S2 by the flux ratio Sgr A*/S2 obtained from the fit in each extracted image. The calculated S2 spectrum used is νS_ν for a blackbody with a temperature of 25,000K, and a stellar radius of 9.3 $R_\odot$, the best fit temperature and radius for S2 found in Martins et al. (2009). The source is placed at 8.2 kpc (Genzel et al. 2010a) from the Earth. This spectrum is normalized to a value of 20 mJy at 2.2 μm wavelength to match previous photometric measurements of S2. This procedure corrects for the effects of interstellar extinction. Note that by normalizing the spectrum of S2 to a value of 20 mJy at 2.2 μm, we do not take into account the error on the previous measurements of the flux of S2. Since errors on this value result only in an overall error on the amplitude and not in the spectral shape, this additional uncertainty in the normalization of the spectra is taken into account in the later model fits by allowing the overall amplitude of the NIR spectrum to vary and determining the effect of this variation on the fit parameters.

To obtain the final NIR data points used for the model fitting in this paper, the noisy spectrum is binned into 10 spectral bins (median of the values in each bin) of width 35 nm. The error on each point is the standard deviation of the sample, or $\sigma/\sqrt{N}$. We have tested varying the number of initial spectral samples used to create the extracted images used for fitting Sgr A*/S2, and find that it has almost no effect on the final data values and only a small effect on the derived error bars. We have also tried fixing parameters in the fits to determine their effects on the final spectra. We tried fixing the FWHM of the Gaussians and the background level (which both naturally vary with wavelength) to their median values, and found that this affects the spectral index of the final data points by at most a few percents.

3 X-RAY OBSCURATION AND MEAN X-RAY PROPERTIES OF BRIGHT FLARES

We started the study of Sgr A*'s emission by investigating the properties of the absorption-scattering layers that distort its spectrum.

3.1 Dust scattering

Scattering on dust grains along the line of sight can have a significant impact on the observed X-ray spectra (Predehl & Schmitt 1995; Smith et al. 2016). The main effect of dust scattering is to create a halo around the source, by removing flux from the line of sight. Both the flux in the halo and its size decrease with energy (with a dependence of $\propto E^{-2}$ and $\propto E^{-1}$, respectively) as a consequence of the probability of scattering that drops steeply with energy. If the events used to extract the source photons are selected from a small region containing only a small part of the halo, such as typically the case for X-ray observations of Sgr A*, then the spectral shape will be distorted by the effects of dust scattering. Whenever the distortions are not accurately accounted for, this will cause significant biases in the measured absorption column densities, source brightness and spectral slopes (see appendix B).

Frequently used models, aimed at mitigating the effects of dust scattering, are: DUST (Predehl & Schmitt 1995); SCATTER (Porquet et al. 2003; 2008; Dodds-Eden et al. 2009) and; DUSTSCAT (Baganoff et al. 2003; Nowak et al. 2012). In all these models the dust optical depth and therefore the magnitude of the correction, is

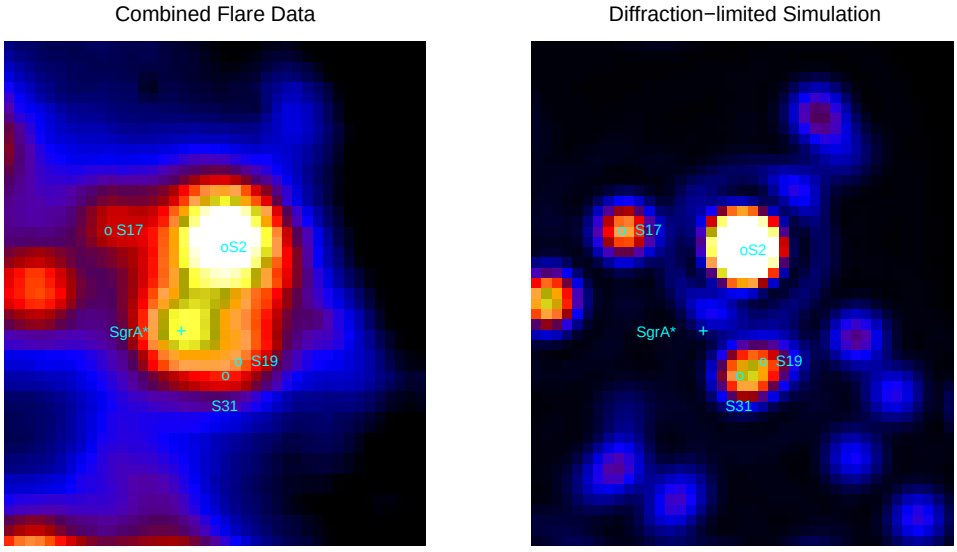

Figure 2. The GC as seen with *SINFONI* (each image is 0.51" × 0.61"). The image on the left is the collapsed image from the spectral range 2.25-2.35 μm for the seven data cubes combined. The image on the right is a diffraction-limited simulated image of the locations of the S-stars in the GC. In both images the location of Sgr A* is indicated with a cross, and the four stars included in our Gaussian fits for spectrum extraction are labeled with circles. The flare is clearly visible above the background in the left image.

Spec	t_{start} BJD_{TBD}	t_{stop} BJD_{TDB}	Γ	$F_{2.2\mu m}$† (mJy)
IR1	2456900.47470	2456900.48164	1.48 ± 0.23	8.87 ± 0.10
IR2	2456900.48971	2456900.49665	1.37 ± 0.19	7.91 ± 0.07
IR3	2456900.49694	2456900.50388	1.80 ± 0.13	10.09 ± 0.07
IR4	2456900.52160	2456900.52855	1.76 ± 0.21	7.52 ± 0.06
IR5	2456900.53675	2456900.54370	3.71 ± 0.48	3.12 ± 0.07
IR6	2456900.54398	2456900.55093	2.72 ± 0.23	4.23 ± 0.04
IR7	2456900.55914	2456900.56608	2.56 ± 0.21	7.07 ± 0.06

Table 3. The second and third column show the Barycentre corrected start and end times of each of the seven *SINFONI* spectra. Times are Barycentric Julian Dates in Barycentric Dynamical Time. The last two columns show the test fit photon index (Γ) and flux once the *SINFONI* data are fitted with a simple power-law model. †The error bars are statistical only and they do not include systematic effects due to spectral extraction. The effect of systematics is treated in §5.3.4.

assumed to be proportional to the X-ray absorbing column density, with a factor derived from Predehl & Schmitt (1995). The underlying assumption is that the dust properties (e.g., dust to gas ratio, size distribution, composition, etc.) towards Sgr A* are equal to the average estimate derived from the study of all the Galactic sources considered in the work of Predehl & Schmitt (1995). After considering the limitations of this approach, we decided to use a completely different method.

Thanks to the analysis of all the *XMM-Newton* and *Chandra* observations of the GC, Jin et al. (2016) just completed the accurate characterisation of the dust scattering halo towards AX J1745.6-2901, a bright X-ray binary located only $\sim 1.45'$ from Sgr A*. The authors deduced that 74 ± 7 % of the dust towards AX J1745.6-2901 resides in front of the GC (e.g. in the spiral arms of the Galaxy). Moreover, the detailed modelling of the dust scattering halo allowed Jin et al. (2016) to provide an improved model of the spectral distortions generated by the dust scattering (FGCDUST), without the requirement to assume fudge scaling factors. We therefore decided to fit Sgr A*'s spectrum with the FGCDUST model, implicitly assuming that the dust has similar properties along the line of sight towards Sgr A* and the foreground component in the direction of AX J1745.6-2901. This is corroborated by the study of the radial and azimuthal dependence of the halo. In fact, the smoothness of the profile indicates that the foreground absorption has no major column density variations within $\sim 100 - 150''$ from AX J1745.6-2901 (Jin et al. 2016). Further details on the spectral distortions (and their correction) introduced by dust scattering are discussed in Appendix B.

3.2 Foreground absorption towards the bright sources within the central arcmin

We review here the measurements of the X-ray column density of neutral/low-ionised material along the line of sights towards compact sources located close to Sgr A*. Due to the variety of assumptions performed in the different works (e.g., absorption models, abundances, cross sections, dust scattering modelling, etc.), we decided to refit the spectra to make all measurements comparable with

the abundances, cross sections and absorption models assumed in this work (see §2.1; Fig. 5 and Tab. 2 of Ponti et al. 2015 and Ponti et al. 2016).

AX J1745.6-2901 located at $\sim 1.45'$ from Sgr A*

AX J1745.6-2901 is a dipping and eclipsing neutron star low mass X-ray binary (Ponti et al. 2016). Such as typically observed in high inclination low mass X-ray binaries, AX J1745.6-2901 shows both variable ionised and neutral local absorption (Ponti et al. 2015). The total neutral absorption column density towards AX J1745.6-2901 has been measured by Ponti et al. (2015b). We re-fitted those spectra of AX J1745.6-2901 with the improved correction for the dust scattering distortions. By considering that only 74 ± 7 % of the dust towards AX J1745.6-2901 resides in front of the GC (Jin et al. 2016), we measured a total column density in the foreground component[6] of $N_H = (1.7 \pm 0.2) \times 10^{23}$ cm^{-2}. We note that the halo associated to the foreground component is still detected at radii larger than $r > 100''$ (Jin et al. 2016), therefore from a radius more than ten times larger than the one chosen to extract Sgr A*'s photons, indicating that a careful treatment of the distortions introduced by dust scattering is essential.

SWIFT J174540.7-290015 located at $\sim 16''$ from Sgr A*

A deep *XMM-Newton* observation performed during the recent outburst of Swift J174540.7-290015 (Reynolds et al. 2016), allowed Ponti et al. (2016) to measure the column density along this line of sight and to find $N_H = (1.70 \pm 0.03) \times 10^{23}$ cm^{-2}, by fitting the spectrum with the sum of a black body plus a Comptonisation component[7]. By applying the improved modelling of the dust scattering halo to the same data, we measured a column density of $N_H = (1.60 \pm 0.03) \times 10^{23}$ cm^{-2}.

SGR J1745-2900 located at $\sim 2.4''$ from Sgr A*

SGR J1745-2900 is a magnetar located at a small projected distance from Sgr A* (Mori et al. 2013; Kennea et al. 2013), and it is most likely in orbit around the supermassive BH (Rea et al. 2013). Coti-Zelati et al. (2015) fitted the full *XMM-Newton* and *Chandra* dataset available on SGR J1745-2900, without considering the effects of the dust scattering halo, and found $N_H = (1.90 \pm 0.02) \times 10^{23}$ cm^{-2} for *Chandra* and $N_H = (1.86^{+0.05}_{-0.03}) \times 10^{23}$ cm^{-2} for *XMM-Newton*. We refitted the *XMM-Newton* dataset at the peak of emission (obsid: 0724210201), using as background the same location when the magnetar was in quiescence and considering the improved dust model, and we obtained $N_H = (1.69^{+0.17}_{-0.10}) \times 10^{23}$ cm^{-2}.

Radio observations of the pulsed emission from SGR J1745-2900 allowed Bower et al. (2014) to provide a full characterisation of the scattering properties of the absorption. The authors found the obscuring-scattering layer to be located in the spiral arms of the Milky Way, most likely at a distance $\Delta = 5.8 \pm 0.3$ kpc from the GC (however a uniform scattering medium was also possible). Moreover, the source sizes at different frequencies are indistinguishable from those of Sgr A*, demonstrating that SGR J1745-2900 is located behind the same scattering medium of Sgr A*.

We note that the column densities of absorbing material along the line of sights towards SWIFT J174540.7-290015, SGR J1745-2900 and the foreground component towards AX J1745.6-2901 are consistent (to an uncertainty of $\sim 2 - 10$ %) within each other. Of course, the neutral absorption towards these accreting sources might even, in theory, be local and variable (e.g. Diaz-Trigo et al. 2006; Ponti et al. 2012; 2016b), however the similar values observed in nearby sources indicate a dominant ISM origin. We note that the location of the scattering medium towards Sgr A* and the foreground component of AX J1745.6-2901 are also cospatial. This suggests that all these sources are absorbed by a common, rather uniform, absorbing layer located in the spiral arms of the Milky Way (Bower et al. 2014; Jin et al. 2016). This result is also in line with the small spread, of the order of $\sim$ 10 %, in the extinction observed in NIR towards the central $\sim 20''$ of the Galaxy (Schödel et al. 2010; Fritz et al. 2011). Indeed, for a constant dust to gas ratio, this would induce a spread in the X-ray determined N_H of a similarly small amplitude. In addition to this layer, AX J1745.6-2901 also shows another absorbing component, located closer to the source, possibly associated either with the clouds of the central molecular clouds or a local absorption (Jin et al. 2016).

Studies of the scattering sizes from large scale ($\sim 2^\circ$) low frequency radio maps also agree with the idea that the intervening scattering in the GC direction is composed of two main absorption components, one uniform on a large scale and one patchy at an angular scale of $\sim 10'$ and with a distribution following the clouds of the central molecular zone (Roy 2013).

3.3 The mean spectra of the *XMM-Newton* very bright flares

We extracted an EPIC-pn and -MOS spectra for each of the bright and very bright flares detected by *XMM-Newton*. We used a Bayesian block decomposition of the EPIC-pn light curve to define the start and end flare times (see Tab. 1). We fitted each spectrum with a power-law model modified by neutral absorption (see §2.1) and by the contribution from the dust scattering halo (FGCDUST * TBNEW * POWER-LAW in XSPEC).

Each spectrum is well fitted by this simple model (see Tab. 4). In particular, the column density of absorption material and the photon index are consistent with being the same between the different flares and consistent with the values observed in nearby sources (see §3.2). This agrees with the idea that most of the neutral absorption column density observed towards Sgr A* is due to the interstellar medium (ISM). If so, the absorption should not vary significantly over time (see Tab. 4). Therefore, we repeat the fit of the spectra assuming that the three very bright flares are absorbed by the same column density of neutral material. The three spectra are well described by this simple model (see Tab. 4), significantly reducing the uncertainties. The best fit spectral index is $\Gamma_{VB123} = 2.20 \pm 0.15$, while the column density is: $N_H = (1.59 \pm 0.15) \times 10^{23}$ cm^{-2}.

This value is fully consistent with the one observed towards the foreground component towards bright nearby X-ray sources, reinforcing the suggestion that the column density is mainly due to the ISM absorption. For this reason hereafter we will fix it to the most precisely constrained value $N_H = 1.60 \pm 0.03 \times 10^{23}$ cm^{-2} (Ponti et al. 2016b). The resulting best fit photon index with this value of N_H is $\Gamma_{VB123_{FixN_H}} = 2.21 \pm 0.09$.

4 MEAN PROPERTIES OF VB3

We investigate here the mean properties of a very bright flare (VB3, see Ponti et al. 2015a) during which, for the first time, simultaneous time-resolved spectroscopy in NIR and X-rays has been measured.

[6] The large uncertainty in this measurement is driven by the uncertainty in the determination of the fraction of column density in the foreground component.

[7] The authors find marginal evidence for sub-Solar iron abundance, suggesting that iron is depleted into dust grains. The detailed investigation of the metal abundances is beyond the scope of this paper.

Absorbed power-law fit to X-ray spectra				
Name	N_H	Γ_X	Flux$_{2-10}$	χ^2/dof
VB1	1.6 ± 0.2	2.2 ± 0.3	9.6^{+7}_{-4}	89.9/114
VB2	1.6 ± 0.3	2.3 ± 0.4	$5.0^{+5}_{-2.4}$	89.3/98
VB3	1.6 ± 0.3	2.3 ± 0.3	$7.6^{+7.1}_{-3.4}$	127.2/117
VB123†	1.59 ± 0.15	2.20 ± 0.15		302.8/331
VB123$_{FixN_H}$‡	1.6	2.21 ± 0.09		302.8/332
VB3$_{XMM+Nu}$‡	1.6	2.27 ± 0.12	7.5 ± 1.5	141.4/133

Table 4. Best fit parameters of the fit of the very bright flares of Sgr A⋆. Column densities are given in units of 10^{23} cm^{-2} and the absorbed fluxes are in units of 10^{-12} erg cm^{-2} s^{-1}. †The VB123 flare indicates the average of VB1+VB2+VB3. ‡The VB123$_{FixN_H}$ shows the best fit results of flare VB123, once the column density of neutral absorbing material has been fixed. The VB3$_{XMM+Nu}$ shows the best fit results of flare VB3 (by fitting both *XMM-Newton* and *NuSTAR* data), once the column density has been fixed.

4.1 X-ray (*XMM-Newton* and *NuSTAR*) mean spectra of VB3

We first simultaneously fitted the *XMM-Newton* (pn and both MOS) and *NuSTAR* mean spectra of VB3 (see Fig. 3, Tab. 1) with an absorbed power law model. The *NuSTAR* data cover only part of the flare, missing the decaying flank of the flare, therefore probing different stages of a variable phenomenon. We accounted for this by allowing the fit to have different power-law normalisation between the *NuSTAR* and *XMM-Newton* spectra[8]. The best fit photon index is: $\Gamma_{XMM+Nu} = (2.27 \pm 0.12)$ and absorbed 2-10 keV flux $F_{2-10} = 7.5 \pm 1.5 \times 10^{-12}$ erg cm^{-2} s^{-1}. The spectra were very well fit by this simple model with $\chi^2 = 141.4$ for 133 dof.

We investigated for the presence of a possible high-energy cut-off (or high-energy spectral break) by fitting the spectra with an absorbed broken power-law model. We fixed the photon index of the lower energy power-law slope to $\Gamma_{VB123_{FixN_H}} = 2.20$ (the best fit value of the simultaneous fit of VB1+VB2+VB3, see Tab. 4). No significant improvement was observed ($\chi^2 = 141.2$ for 132 dof).

4.2 Multi-wavelength mean spectra of VB3

We then extended our investigation by adding the NIR spectra. Multiple *SINFONI* spectra (e.g., IR2, IR3 and IR4) have been accumulated during the duration of the X-ray emission of the VB3 flare[9] (see Fig. 5). Therefore, we created the mean spectrum from these NIR spectra and fitted these simultaneously with the mean X-ray spectra of VB3 (see Tab. 3 and Fig. 5).

4.2.1 Single power-law (plain Synchrotron)

We started fitting the mean spectrum from NIR to hard X-ray with a simple power-law model, as expected in the case of plain Synchrotron emission (Dodds-Eden et al. 2009). The best fit photon index was $\Gamma = 2.001 \pm 0.005$ (see Tab. 5 and Fig. 4). However, this very simple model provided us with an unsatisfactory result ($\chi^2 = 189.7$ for 142 dof; Tab. 5). This is mainly driven by the different slopes observed in the NIR and X-ray bands (see Fig. 1 and 4). We therefore concluded that a plain Synchrotron model is ruled out.

[8] The normalisations are, however, consistent between the two instruments.

[9] Defined on the basis of the X-ray light curve, therefore it represents the full duration of the X-ray flare.

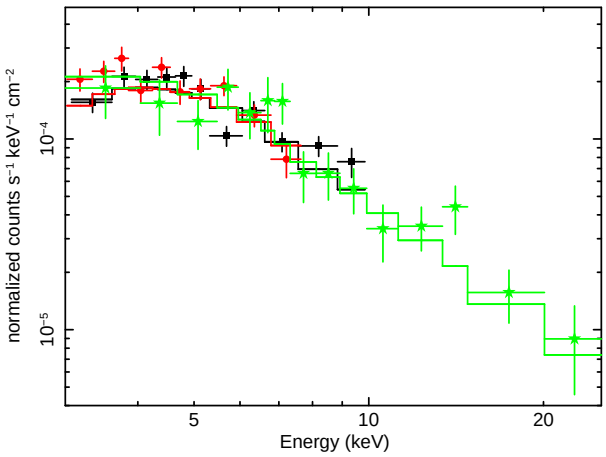

Figure 3. Mean X-ray spectrum of VB3. The black squares, red circles and green stars show the EPIC-pn, combined EPIC-MOS and combined *NuSTAR* spectra, respectively. The combined *XMM-Newton* and *NuSTAR* spectra greatly improve the determination of the X-ray slope. The data are fitted with an absorbed power law model, which takes into account the distortions induced by the dust scattering (see text for more details).

VB3 mean spectrum				
	Single PL	BPL	TSSC	PLCool
Γ_{NIR}	2.001 ± 0.005	1.7 ± 0.1		1.74 ± 0.08
Γ_X		2.27 ± 0.12		
$\Delta\Gamma$		0.57 ± 0.15		0.5
Log(B)		0.94 ± 0.16	4.0 ± 0.4	0.94 ± 0.16
Θ_e			9 ± 4	
Log(N_e)			39.5 ± 0.5	
Log(R$_F$)			-3.5 ± 0.5	
χ^2/dof	189.7/142	154.9/140	162.7/139	156.8/141

Table 5. Best fit parameters of the mean spectrum of VB3 with the Single PL (plain synchrotron), BPL (broken power-law), TSSC (thermal synchrotron self Compton) and PLCool (power-law cool) models. See §4 for a description of the parameters.

4.2.2 Broken power-law model (BPL, phenomenological model)

We then performed a phenomenological description of the data with a broken power-law (BPL) model. We observed a significant improvement and an acceptable description of the spectrum by fitting the data with this model, where the NIR and X-ray slopes were free to vary ($\chi^2 = 154.9$ for 142 dof, $\Delta\chi^2 = 34.8$ for the addition of 2 dof, corresponding to an F-test probability of $\sim 7 \times 10^{-7}$; Tab. 5, Fig. 4). The resulting best fit NIR and X-ray photon indexes are $\Gamma_{NIR} = 1.7 \pm 0.1$ and $\Gamma_X = 2.27 \pm 0.12$, respectively (Tab. 5). The spectral steepening $\Delta\Gamma = 0.57 \pm 0.15$ (± 0.09 at 1-σ) is slightly steeper, but fully consistent with the value expected in the Synchrotron scenario in the presence of a cooling break ($\Delta\Gamma = 0.5$), strongly suggesting this latter scenario as the correct radiative mechanism.

4.2.3 Thermal Synchrotron Self Compton (TSSC)

Before fitting the VB3 mean spectrum with a Synchrotron model with a cooling break, we considered an alternative interpretation, where the NIR band is produced via synchrotron radiation by a thermal distribution of electrons. Moreover, the same population of electrons generates via inverse Compton the high-energy (e.g. X-ray) emission (see e.g. Dodds-Eden et al. 2011). We called this model thermal Synchrotron self Compton (TSSC). The free parameters in this model are: B, the strength of the magnetic field; θ_E, the dimensionless electron temperature (defined as $\theta_E = \frac{kT_e}{m_e c^2}$, where k is the Boltzman constant, T_e is the temperature of the thermal electrons, m_e is the electron mass and c is the speed of light); N, the total number of NIR synchrotron emitting electrons; and R_F, the size of the region containing the flaring electrons, controlling the photon density of the seed photons. The very short variability time-scale (of the order of 10^2 s) suggests a very compact source with a size of the order of (or smaller than) a few Schwarzschild radii, likely located within or in the proximity of the hot accretion flow of Sgr A*. Radio and sub-mm observations constrain the physical parameters of the steady emission from the inner hot accretion flow (within the central ~ 10 R$_S$) to be $B \sim 10 - 50$ G, $T_e \sim 10^{10}$ K, $\gamma_e \sim 10$; $n_e \sim 10^6$ cm^{-3} (see § 1; Loeb & Waxman 2007; Genzel et al. 2010). These are likely the pre-flare plasma conditions.

The TSSC model provides an acceptable fit to the data ($\chi^2 = 162.7$ for 139 dof; see Fig. 4)[10]. However, as observed in previous very bright flares (Dodds-Eden et al. 2009), the best fit parameters of this model are very different from the reasonable range expected to be present in the accretion flow of Sgr A*. Indeed, this model produces the flare via a magnetic field with a staggering intensity of $Log(B) = 4.0 \pm 0.4$ G, about three orders of magnitude larger than the magnetic field intensity within the steady hot accretion flow of Sgr A*, on a population of "not-so-energetic" ($\theta_E = 9 \pm 4$) electrons. Moreover, in order to make the inverse Compton process efficient enough to be competitive to synchrotron, the electron density has to be as high as $n_e = 10^{13}$ cm^{-3}, about seven orders of magnitude higher than in the accretion flow. This appears unlikely. The total number of TSSC emitting electrons is constrained by the model to be $Log(N_e) = 39.5 \pm 0.5$, therefore to reach such an excessively high electron density, the size of the emitting region has to be uncomfortably small, $Log(R_F/R_S) = -3.5 \pm 0.5$. Such a source would be characterised by a light crossing time of the order of only ~ 10 ms. Indeed, variability on such time-scales are typically observed in accreting X-ray binaries (e.g., Belloni et al. 2002; De Marco et al. 2015), where the system is $\sim 10^6$ times more compact than in Sgr A* (Czerny et al. 2001; Gierlinski et al. 2008; Ponti et al. 2012b), while Sgr A*'s power spectral density appears dominated by variability at much larger time-scales (Do et al. 2009; Meyer et al. 2009; Witzel et al. 2012; Hora et al. 2014)[11]. Again, this appears as a weakness of this model.

As already discussed in Dodds-Eden et al. (2009; 2010; 2011) and Dibi et al. (2014; 2016), these physical values are different by several orders of magnitude from the ones observed in quiescence and, therefore they appear unlikely. With this study we show that the same "unlikely" physical parameters are not only observed during VB2 (the flare analysed by Dodds-Eden et al. 2009), but also during the very bright flare considered here (VB3). This confirms that this model produces unreasonable parameters for part (if not all) of the bright flares.

4.2.4 Synchrotron emission with cooling break (PLCool)

In this scenario, the synchrotron emission is produced by a non-thermal distribution of relativistic electrons, embedded in a magnetic field with strength B, therefore they radiate synchrotron emission. At the acceleration site, the injected electrons are assumed to have a power-law distribution in γ_e with index p (i.e. $N(\gamma_e) \propto \gamma_e^{-p}$), defined between γ_{min} and γ_{max} (γ_e being the electron Lorentz factor). We assume as lower boundary $\gamma_{min} = 10$, supposing that the radiating electrons are accelerated from the thermal pool producing the sub-mm peak in quiescence (Narayan et al. 1998; Yuan et al. 2003). We also assume that at any point during the flare, the engine is capable of accelerating electrons to $\gamma_{max} > 10^6$, so that they can produce X-ray emission via synchrotron radiation (this appears as a less reliable assumption and indeed an alternative to this scenario will be discussed in § 8.3).

A well known property of high-energy electrons radiating via synchrotron emission is that they cool rapidly, quickly radiating their energy on a time-scale $t_{cool} = 220(B/50\ G)^{-3/2}(\nu/10^{14}\ Hz)^{-1/2}$ s (where ν is the frequency of the synchrotron emitted radiation; see Pacholczyk 1970). In particular, higher energy electrons cool faster than the NIR ones. The competition between synchrotron cooling and particle escape from the acceleration zone then generates a break in the synchrotron spectrum at a frequency: $\nu_{br} = 2.56(B/30\ G)^{-3}(t_{esc}/300\ s)^{-2} \times 10^{14}$ Hz. Furthermore, in case of continuous acceleration, a steady solution exists where the slope of the power-law above the break is steeper by $\Delta\Gamma = 0.5$ (Kardashev et al. 1962) than the lower energy power-law[12]. Following the nomenclature of Dodds-Eden et al. (2009), we call this model "PLCool". The free parameters of the PLCool model are: B; p; and the normalisation.

As described in §4.2.2 a broken power-law model provides an excellent fit to the mean VB3 multi-wavelength spectrum ($\chi^2 =$

[10] The fits have been performed in MATLAB, implementing the equations reported in Dodds-Eden et al. (2009) and references therein. The best fit was computed through a χ^2 minimisation technique. The parameter space to determine the uncertainties on the best fit parameters has been explored through a Bayesian Markov Chain Monte Carlo approach.

[11] An excessively compact source with such high densities and magnetic field is hardly achievable event through compression of a fraction of the quiescent electrons. The quiescent density of electrons ($n_e = 10^6$ cm^{-3}) dictates that $N_e = 10^{39.5}$ electrons are contained within a sphere of ~ 0.07 R$_S$, that therefore would need to be compressed by 2.3 orders of magnitude to reach the required TSSC source size and density. We note that, assuming conservation of the magnetic flux, the magnetic field strength would rise to $Log(B) \sim 6.2$, two orders of magnitude higher than the best fit value. The magnetic energy would also rise, but would still be 2-4 orders of magnitude smaller than the one required to power the flare.

[12] Synchrotron radiation from the cooling power-law distribution of electrons (with electron power-law index p) generates a spectrum $\nu F_\nu \propto \nu^{(3-p)/2}$ at frequencies lower than the cooling break and $\nu F_\nu \propto \nu^{(2-p)/2}$ above. This implies that p relates to the photon index Γ such as: $\Gamma = \frac{p+1}{2}$ below and $\Gamma = \frac{p+2}{2}$ at frequencies above the cooling break.

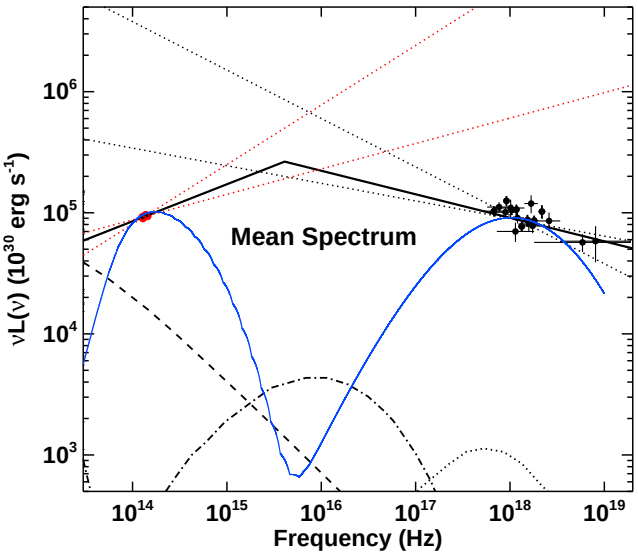

Figure 4. The red and black points show the mean NIR (*SINFONI*) and X-ray (*XMM-Newton* and *NuSTAR*) emission during the VB3 flare. The dotted red and black straight lines show the uncertainties on the determination of the NIR and X-ray power-law slope (with model BPL), respectively. The solid line shows the best fit PLCool model that imposes $\Gamma_X = \Gamma_{NIR}+0.5$. The X-ray slope is slightly steeper ($\Delta\Gamma = 0.57 \pm 0.09$, 1σ), although consistent with the predictions of the PLCool model. Both X-ray and NIR data and models have been corrected for absorption and the effects of dust scattering halo. The blue solid line shows the best fit TSSC model (§5.3.3). For a description of the other lines see Fig. 1.

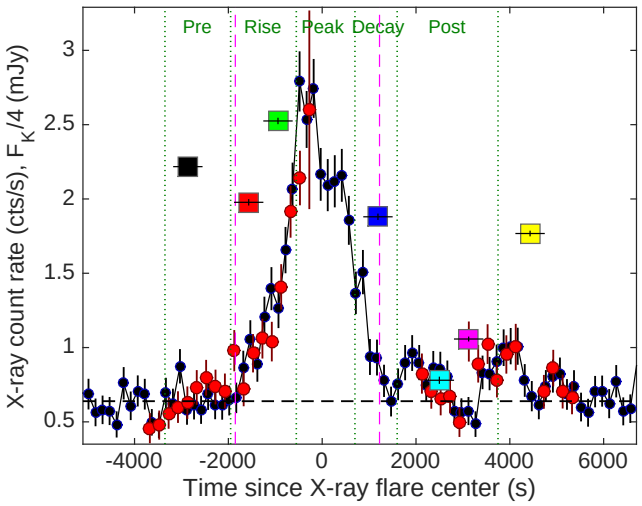

Figure 5. The black and red points show the *XMM-Newton* 2-10 keV (sum of the three EPIC cameras) and *NuSTAR* 3-20 keV light curve of Sgr A⋆'s flare VB3 (Ponti et al. 2015), respectively. A constant rate of 0.13 cts s^{-1} has been subtracted from the *NuSTAR* light curve for display purposes, to take into account the different contribution of the diffuse and quiescent emission (gaps in the *NuSTAR* light curve are due to Earth occultation). The squares show the extinction corrected *SINFONI* light curve of Sgr A⋆ during the VB3 flare. Each point corresponds to a NIR spectrum integration time of 600 s. The y-axis reports the observed renormalised (divided by 4 for display purposes) flux density at 2.2 μm in mJy units. The black dashed line indicates the level of the "non-flare" (quiescent in X-rays) emission. The pink dashed lines indicate the start and end of the *XMM-Newton* VB3 flare, as indicated by the Bayesian block decomposition (see Ponti et al. 2015a). Excess X-ray emission is observed $\sim$ 2000 and $\sim$ 4000 s after the X-ray flare peak. The dotted green lines show the intervals for the integration of the pre-, rise, peak, decrease and post-flare spectra during VB3. The zero point of the abscissa corresponds to 525831144.7 s (TT_{TBD}) and 2456900.50784 day (BJD_{TBD}), respectively.

154.9 for 140 dof). In particular, we note that the difference between the NIR and X-ray photon indices $\Delta\Gamma = 0.57\pm0.15$ (±0.09 at 1-σ) is consistent with the value expected by the PLCool model ($\Delta\Gamma = 0.5$; due to synchrotron emission with continuous acceleration). Indeed, imposing such spectral break ($\Gamma_X = \Gamma_{NIR} + 0.5$), the fit does not change significantly ($\chi^2 = 156.8$ for 141 dof), with the photon index $\Gamma_{NIR} = 1.74 \pm 0.08$ and the break at $0.04^{+0.12}_{-0.03}$ keV ($B = 8.8^{+5.0}_{-3.0}$ G; Fig. 4). We note that the PLCool model provides a significantly better fit ($\chi^2 = 156.8$) than the TSSC model ($\chi^2 = 161.3$) despite having two fewer free parameters (Tab. 5).

To investigate the effects of potential uncertainties on the normalisation of the NIR emission, we artificially increased (and decreased) the *SINFONI* spectrum by a factor 1.25 (and 0.75). The statistical quality of the fit does not change ($\chi^2 = 156.8$ for 141 dof, in all cases), and neither does the best fit photon index, $\Gamma_{NIR} = 1.74 \pm 0.08$. As expected, the main effect of the higher (lower) NIR normalisation is to shift the break towards lower (higher) energies, i.e. $E_{br} = 0.018^{+0.071}_{-0.014}$ keV ($E_{br} = 0.046^{+0.20}_{-0.037}$ keV), corresponding to $B = 11.7^{+8.5}_{-3.3}$ G ($B = 8.5^{+5.5}_{-3.0}$ G).

5 EVOLUTION DURING VB3

5.1 Light curves of VB3

The black and red points in Fig. 5 show *XMM-Newton* and *NuSTAR* light-curves of VB3 in the 2-10 keV and 3-20 keV bands, respectively. The black dashed line indicates the level of diffuse and quiescent emission observed by *XMM-Newton*. For display purposes, we subtracted a constant rate of 0.13 cts s^{-1} from the *NuSTAR* light curve, to take into account the different contribution of the diffuse and quiescent emission. The squares in Fig. 5 show the NIR light-curve as observed with *SINFONI*. Despite the sparse sampling of the light curve allowed by the *SINFONI* integral field unit, it is clear from Fig. 5 that for VB3 the NIR flare lasts longer than the X-ray one. In particular, the NIR flare is already in progress during our first *SINFONI* integration, $\sim 10^3$ s before the start of the X-ray flare and it is still in progress at the end of IR4, with a duration longer than 3.4 ks (see Fig. 5, Tab. 1 and 3). This is not surprising, indeed, a similar trend has already been observed by Dodds-Eden et al. (2009) and Trap et al. (2011) in the only other very bright flare with simultaneous NIR coverage (see Fig. 3 of Dodds-Eden et al. 2009). The pink dashed lines in Fig. 5 indicate the start and end of the *XMM-Newton* VB3 flare as determined by the Bayesian block decomposition (see Ponti et al. 2015a). The dotted green lines indicate the periods during which VB3-Pre, VB3-Rise, VB3-Peak, VB3-Dec and VB3-Post, have been integrated (Tab. 1).

5.2 NIR spectral evolution during VB3

We fit all the seven high quality *SINFONI* spectra (see top panel of Fig. 6) with a simple power-law model, normalised at 2.2 μm (PEGPWRLW). The fit with this simple model provides a $\chi^2 = 96.8$ for 56 dof. The bottom panel of Fig. 6 shows the best fit photon index (Γ_{NIR}, where $\Gamma = 1 - \alpha$ and α is the spectral index $F_\nu \propto \nu^\alpha$) as a function of the flux density (in mJy) at 2.2 μm.

During the *SINFONI* observations the 2.2 μm flux density ranges from ~ 3 to ~ 10 mJy, spanning the range between a classical dim and bright NIR period (Bremer et al. 2011). This suggests that this very bright X-ray flare is associated with a very bright NIR flux excursion. In agreement with previous results, we observe a photon index consistent with $\Gamma_{NIR} = 1.6$ above ~ 7 mJy (solid line in Fig. 6; Hornstein et al. 2007; Witzel et al. 2014). On the other hand, Fig. 6 also shows steeper NIR spectral slopes at low fluxes. We note that steep NIR slopes at low fluxes have been already reported (Eisenhauer et al. 2005; Gillessen et al. 2006; Bremer et al. 2011), however recent observations by Witzel et al. (2014) indicate no spectral steepening at low fluxes. The results of our work appear to suggest an evolution of the spectral slope at low fluxes during and after this very bright X-ray flare, however higher quality data are necessary to finally clarify this trend.

5.3 Multi-wavelength spectral evolution during VB3

We extracted strictly simultaneous *XMM-Newton* and *NuSTAR* spectra for each of the 7 NIR *SINFONI* spectra (see Fig. 10). All are covered by *XMM-Newton* and *NuSTAR*, apart from spectrum IR4, for which Sgr A* was not visible by *NuSTAR* at that time (due to Earth occultation). The first four (from IR1 to IR4) of these spectra have been accumulated either when the X-ray counterpart of VB3 was visible or in its close proximity and they all show bright NIR emission, therefore we present the results of the analysis of those "flaring spectra" here. The remaining three, associated with faint NIR and X-ray quiescent emission, are investigated in the next section (§6).

We stress again that during the IR1 spectrum the flare was already very bright ($F_{2.2\mu m} \sim 9$ mJy) in the NIR band, while only upper limits were observed in X-rays (see Fig. 5 and 7). Indeed, the X-ray flare started roughly 20 min later, during IR2, and peaked just after IR3. Bright NIR emission with no X-ray counterpart in the early phases of the flare places tight constraints on the PLCool model (see §8). During IR4 the NIR flux was still high ($F_{2.2\mu m} \sim 7.5$ mJy), while the X-ray flare was about to end (Fig. 5). After IR4 the NIR droped significantly and the X-ray emission returned to the quiescent level.

5.4 Is the spectral evolution required?

We started the time-resolved spectral analysis by testing whether the data require any spectral evolution during VB3. We therefore simultaneously fitted the multi-wavelength flaring spectra (IR1, IR2, IR3 and IR4) with a broken power law model, forcing the NIR and X-ray photon indexes and the break energy to be constant over time. This provides an unacceptable fit ($\chi^2 = 237.6$ for 104 dof), demonstrating that significant spectral variability is required during the flare. The best fit photon indexes are $\Gamma_{NIR} = 1.71 \pm 0.09$, $\Gamma_X = 2.21 \pm 0.10$, with the break at $E_{br} = 10^{+150}_{-3}$ eV. We note that, similar to what has been found in the analysis of the mean spectrum, the spectral steepening is $\Delta\Gamma = 0.50 \pm 0.13$, therefore perfectly consistent with $\Delta\Gamma = 0.5$.

We then refitted the spectra with the same model, allowing the NIR photon index and the break energy to evolve with time, while imposing the X-ray photon index to be $\Gamma_X = \Gamma_{NIR} + 0.5$. This provided a significant improvement to the fit ($\Delta\chi^2 = 97.6$ for the addition of 5 new parameters), demonstrating that Sgr A*'s spectrum changed shape during VB3. Indeed, we observe best fit photon indexes of: $\Gamma_{NIR1} = 1.70 \pm 0.05$, $\Gamma_{NIR2} = 1.60 \pm 0.08$, $\Gamma_{NIR3} = 1.91 \pm 0.07$ and $\Gamma_{NIR4} = 1.81 \pm 0.13$, while the break is at $E_{br1} = 0.6 \pm 0.03$, $E_{br2} = 0.9 \pm 0.03$, $E_{br3} = 1150^{+1800}_{-800}$ and $E_{br4} = 14^{+400}_{-11}$ eV. We note that this model can acceptably reproduce the data ($\chi^2 = 140.0$ for 99 dof).

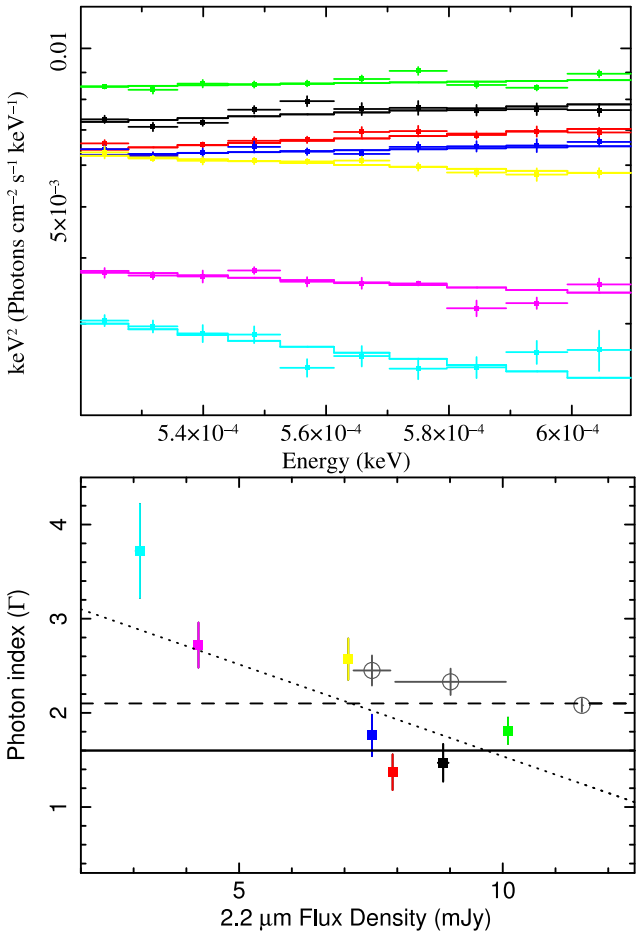

Figure 6. *(Top panel) SINFONI* spectra fitted with a power-law model in the energy band $E \sim 0.525 - 0.608$ eV. The color (black, red, green, blue, cyan, magenta and yellow) indicates the chronological sequence of the spectra. *(Bottom panel)* Best fit photon index (Γ_{NIR}) as a function of the 2.2 μm flux density (in mJy units). The NIR photon indexes are shown with filled squares, with the same color code as before. The empty dark grey circles show the spectral indexes in the 2-10 keV band, during the rise, decay and peak of very bright flares. For these points, we associate to the flare rise and decay X-ray photon indexes the simultaneous NIR fluxes. For the flare peak, we assume a value of 11.5 mJy. The dotted lines show the best fit of the NIR photon indexes with a linear relation. The solid line shows the constant photon index typically observed at medium-high fluxes (flux density > 7 mJy; $\Gamma_{NIR} = 1.6$; Hornstein et al. 2007). The dashed line shows the associated X-ray slope, if the spectrum is dominated by synchrotron emission with a cooling break $\Gamma_X = \Gamma_{NIR} + 0.5$.

5.5 Evolution of the BPL model during VB3

Before considering the PLCool model, where the slopes in NIR and X-rays are tied by the relation $\Gamma_X = \Gamma_{NIR} + 0.5$, we fitted each time-resolved multi-wavelength spectrum with the phenomenological BPL model (§4.2.2), where the slopes in the NIR and X-ray bands are free to vary (Tab. 6).

The NIR slope was always well determined ($\Delta\Gamma_{NIR} \sim 0.2$; see Tab. 6 and 3). On the other hand, the presence of either upper

Simultaneous (600 s) NIR to X-ray spectra during VB3				
		BPL		
	Γ_{NIR}	Γ_X	E_{br} (eV)	χ^2/dof
IR1	1.5 ± 0.2	> 2.2	1‡	20.8/15
IR2	1.4 ± 0.2	3.2 ± 0.4	$0.16^{+0.20}_{-0.11}$	32.8/24
IR3	1.8 ± 0.2	2.57 ± 0.16	420^{+980}_{-210}	43.8/43
IR4	1.8 ± 0.2	2.14 ± 0.02	1‡	11.4/10
		PLCool		
	Γ_{NIR}		E_{br} (eV)	χ^2/dof
IR1	1.72 ± 0.04		0.60 ± 0.03†	23.7/15
IR2	1.58 ± 0.01		0.61 ± 0.03†	43.8/25
IR3	1.87 ± 0.07		530^{+1400}_{-380}	46.0/44
IR4	$1.77^{+0.06}_{-0.02}$		$9.7^{+77}_{-8.0}$	11.2/10
		PLCoolEv		
	Γ_{NIR}	E_c (keV)	E_{br} (eV)	χ^2/dof
IR1	$1.48^{+0.25}_{-0.05}$	$6 \times 10^{-4} - 1$	$0.6 - 1000$	17.4/14
IR2	1.5 ± 0.2	$3.5^{+0.3}_{-1.1}$	$1^{+2}_{-0.5}$	35.6/24
IR3	1.82 ± 0.07	> 9	250^{+780}_{-150}	45.3/43
IR4	$1.77^{+0.06}_{-0.02}$	> 10	$9.8^{+77}_{-8.3}$	11.0/9

Table 6. Best fit parameters of Sgr A*'s emission as fitted during each of the (600 s) *SINFONI* and strictly simultaneous X-ray spectra accumulated during the flare VB3. The spectra are fit with both the BPL, the PLCool and the PLCoolEv models. Γ_{NIR} and Γ_X indicates the power law photon indexes fitting the NIR, the X-ray band, respectively. For the PLCool and PLCoolEv models the Γ_{NIR} indicates the best fit NIR slope, once the total band is fitted with the assumption that $\Gamma_X = \Gamma_{NIR} + 0.5$. E_{br} indicates the energy of the cooling break. E_c indicates the energy of the high-energy cut-off (induced by γ_{max}). †The best fit energy of the break falls right at the higher edge of the *SINFONI* energy band. ‡Unconstrained value, therefore fixed to 1 eV.

limits or low statistics prevented us from determining Γ_X at the same time of E_{br} in spectra IR1 and IR4 (Tab. 6). We, therefore, "a priori" assumed that the breaks in IR1 and IR4 occur at 1 eV (which corresponds to $B = 30$ G, if interpreted as a cooling break). We then constrained the power-law slopes in the X-ray band under this assumption ($\Gamma_X > 2.2$ and $\Gamma_X = 2.14 \pm 0.02$ for IR1 and IR4, respectively). Moving the break to 25 eV (corresponding to $B = 10$ G) the slope would steepen to $\Gamma_X > 2.6$ and $\Gamma_X = 2.4 \pm 0.1$, respectively. For IR2 and IR3, the X-ray data are of good enough quality to have a good constraint on the X-ray slope (see Tab. 6). The dotted lines in the corresponding panels of Fig. 7 show the uncertainties on the X-ray and NIR slopes. The BPL model produced an acceptable description of the spectra (the surviving residuals are due to intrinsic scatter in the NIR band; see Tab. 6).

5.6 Evolution of the PLCool model during VB3

We then fitted the spectra with the PLCool model (Fig. 7; Tab. 6). This model reproduces Synchrotron emission with a cooling break under the assumption that, at any time, $\gamma_{max} > 10^6$.

5.6.1 Successes of the PLCool model

For IR1, IR3 and IR4 the PLCool model provides a good fit to the data of indistinguishable (at 90 % confidence) quality compared to the phenomenological BPL model (Tab. 6). The advantage over BPL is that the PLCool model is physically motivated.

We observed that for all spectra (from IR1 to IR4) the NIR spectra are flat and consistent with being constant (e.g. $\Gamma_{NIR} \sim 1.6$, see Fig. 6) before and during the full duration of the X-ray flare. This is in line with the values typically observed during bright NIR flux excursions (Hornstein et al. 2007)[13]. We also noted that at the peak of the X-ray flare, when the constraints are best, the X-ray slope is steeper than the simultaneous NIR one by $\Delta\Gamma \sim 0.5$, consistent with the one expected by the PLCool model (see Fig. 7 and Tab. 6).

Blindly applying the PLCool model to all time resolved spectra (it might be incorrect to apply the PLCool model when no X-ray emission is detected), we observed a significant evolution of the energy of the cooling break, that implies (under the assumption of a constant escape time) a variation of the strength of the magnetic field (Tab. 6). The black, red, green, blue and grey dotted and solid lines in Fig. 8 show the 68 and 90 % confidence contours of the uncertainty on E_{br} and Γ_{IR} for IR1, IR2, IR3, IR4 and the mean spectrum, respectively. We note that a highly significant evolution of the cooling break is observed. Indeed, during both IR1 and IR2, the break appears to be at very low energy, corresponding to a magnetic field of the order of $B \sim 35$ G. While the energy of the break is significantly higher during IR3, indicating that the magnetic field had significantly reduced around the peak of the X-ray flare ($B = 3.8^{+2.0}_{-1.3}$ G). The energy of the break then drops again in the decreasing flank of the X-ray flare to a value of $E_{br} = 9.7^{+77}_{-8.0}$ eV, corresponding to an increase in the strength of the magnetic field ($B = 14.3^{+11.3}_{-7.4}$ G).

5.6.2 Difficulties of the PLCool model

As we have outlined, the PLCool model (which assumes $\gamma_{max} > 10^6$ at all times) presented many successes. However, we also point out here three severe weaknesses that will be discussed further in the discussion section: i) twice out of four times the cooling break is observed to peg just above the NIR band ($E \sim 0.6$ eV). This appears as a rather unlikely possibility; ii) during IR1, bright and flat ($\Gamma = 1.48 \pm 0.2$) NIR emission is associated to no enhanced X-ray emission ($F_{3-10\ keV} < 2.3 \times 10^{-12}$ erg cm^{-2} s^{-1}). This is hard to reconcile with the PLCool model that, in order to fit this spectrum, pushes the best fit NIR photon index to $\Gamma_{NIR} = 1.72 \pm 0.04$; iii) the very steep X-ray spectrum during IR2 ($\Gamma_X = 3.2 \pm 0.4$) implies a spectral steepening incompatible with the PLCool model ($\Delta\Gamma = 1.8 \pm 0.4$, instead of $\Delta\Gamma = 0.5$).

5.7 Can the TSSC model fit the IR2 spectrum?

In theory SSC models, with a thermal distribution, can produce fairly steep spectral shapes at high energies. Therefore, although the TSSC model produced unreasonable parameter values when applied to the mean VB3 spectrum, we checked whether TSSC might be the dominant radiative mechanism during peculiar and short duration intervals, such as IR2.

The best fit TSSC model was significantly worse than the PLCool model, despite having two more free parameters ($\chi^2 =$

[13] More observations are needed to confirm the tentative hint for a steeper NIR slope in the early phase of the NIR flare (IR1 and IR2 compared to IR3 and IR4; see 6).

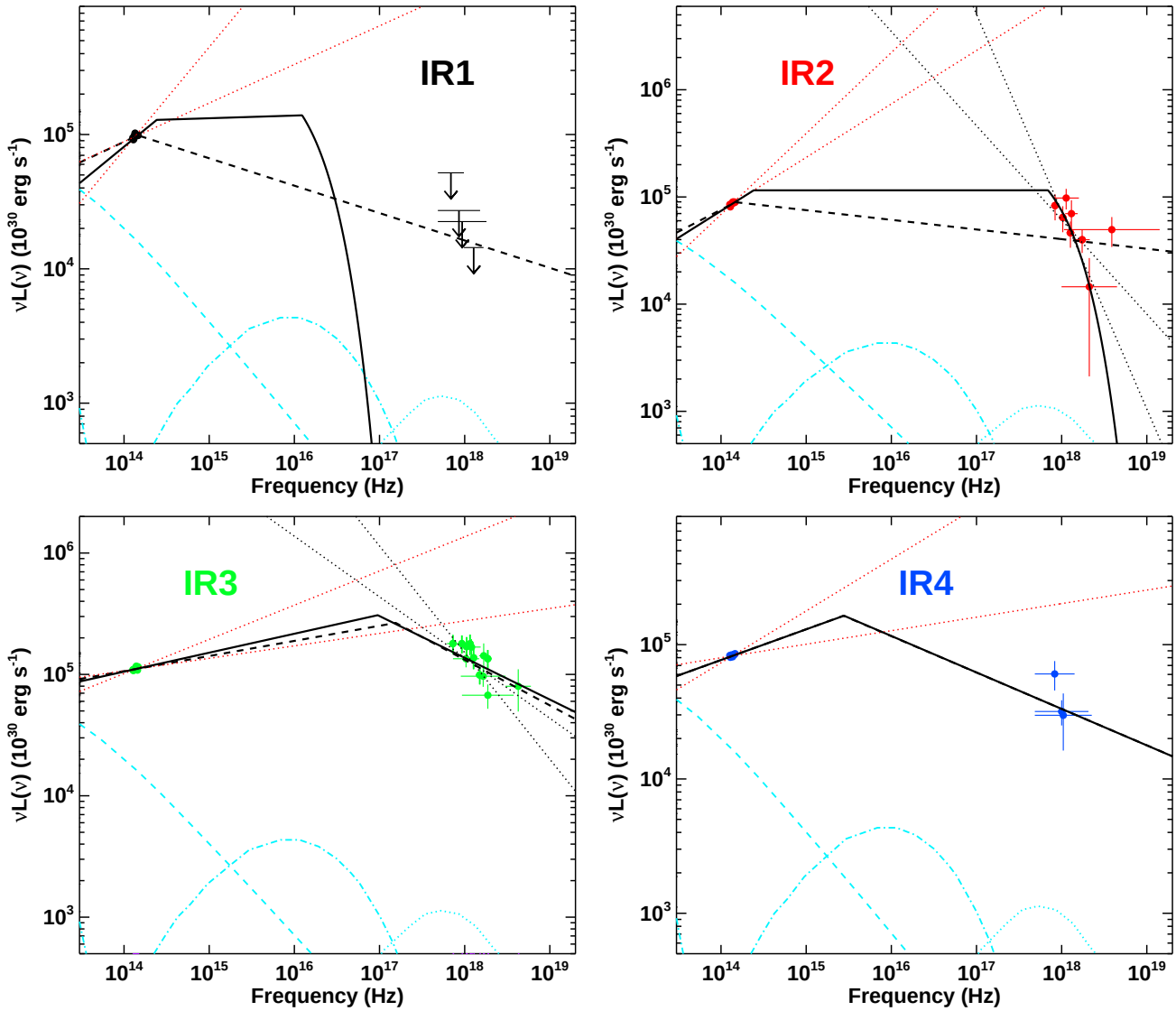

Figure 7. Evolution of Sgr A*'s SED during the very bright flare VB3. Each panel shows the *SINFONI* and simultaneous X-ray spectra fitted with the PLCool model, during each of the 4 *SINFONI* spectra integrated during the VB3 flare (see Fig. 5). The colour code is the same as in Fig. 5, with the temporal sequence: black; red; green and; blue. The red and black dotted lines show the uncertainties in the determination of the NIR and X-ray power-law slopes, respectively. The X-ray slopes are well determined only for the IR2 and IR3 spectra. The black dashed lines show the best fit PLCool models, where $\Gamma_X = \Gamma_{NIR} + 0.5$ is imposed. For IR2 the observed X-ray slope is inconsistent with the predictions of the PLCool model. For both IR1 and IR2 the cooling break is suspiciously pegged in the NIR band. The black solid lines show the best fit PLCoolEv models. During IR1 both the cooling break and the cut-off have large uncertainties, but are constrained to lie within few $10^{14} < \nu < 10^{18}$ Hz. During IR2 the cut-off is in the X-ray band. From IR2 to IR3 the cooling break evolves to higher energies and then back to lower energies during IR4. Sgr A* is undetected in X-rays during observation IR1. Such as in Fig. 4 both data and models are de-absorbed and corrected for the effects of the dust scattering halo. For a description of the other lines see Fig. 1.

60.1 for 23 dof). Indeed, the model failed to produce a better fit because it was mainly constrained by the flat X-ray photon index produced by the TSSC model. In addition, we noted that the fit of IR2 leaded to unreasonable best fit parameters, similar to the ones fitting the mean VB3 spectrum. Indeed, we observed: $Log(B) = 3.55$, $\theta_E = 32.6$, $Log(N_e) = 39.3$ and $Log(R_F/R_S) = -3.0$. Once again the magnetic field strength appears, unreasonably large, the size of the source unreasonably small, and the source density many orders of magnitude higher than expected.

5.8 Synchrotron emission with cooling break and evolving γ_{max} (PLCoolEv)

When we considered the PLCool model, we "a priori" used the assumption that at any time the source can accelerate particles to very high energies $\gamma_{max} > 10^6$. This implies that an engine, able to accelerate electrons to $\gamma_{max} > 10^6$, is created on a negligible time-scale, at the start of the NIR flare. If so, the PLCool model can be applied to the entire duration of the flare (as we performed in §5.6.2).

On the other hand, if the engine has a size of a few Schwarzschild radii, its light (or Alfven speed) crossing time would be of the order of a hundred seconds, comparable to the time-scales

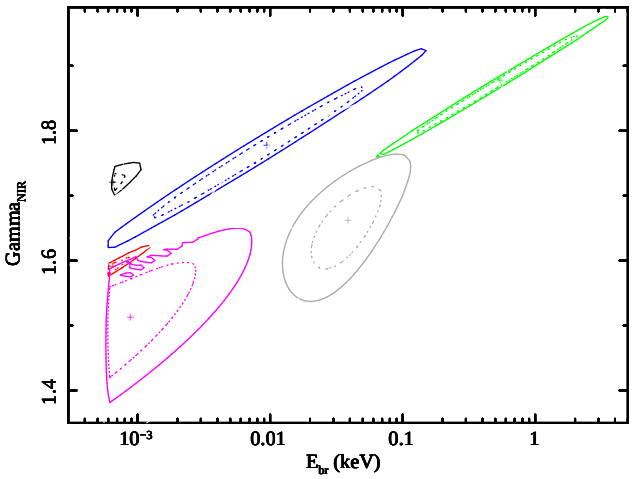

Figure 8. The black, red, green, blue and grey lines show confidence contours of the uncertainty on E_{br} and Γ_{IR} for IR1, IR2, IR3, IR4 and the mean spectrum once fitted with the PLCool model, respectively. The dotted and solid lines show the 68 and 90 % confidence contours, respectively. During IR1 and IR2 the cooling break pegs at its lowest value, being located just above the NIR band. Once fitted with the PLCoolEv model, the confidence contours remain unchanged for IR3, IR4 and the mean spectrum, because during these intervals the high energy cut off is at very high energy. The magenta lines show the confidence contours during IR2, when the cut off is observed in the X-ray band. During IR1, the cut off falls between the NIR and X-ray band, therefore the location of the cooling break is unconstrained.

of the flares under investigation here. Thus, it might be possible that the creation and destruction of the engine occurs on a similar time-scale to the flares and that the engine is initially not powerful enough to accelerate particles to $\gamma_{max} > 10^6$. Based on these considerations, we introduce a new phenomenological model dubbed PLCoolEv, by adding to the PLCool model the freedom of having a variable value of γ_{max}. We performed this by adding a high energy cut off to the PLCool model (reproduced by the HIGHECUT component in XSPEC). Indeed, the PLCoolEv model assumes that γ_{max} evolves during the flare. A low value of γ_{max} (e.g., $\gamma_{max} << 10^6$) would imply that no electrons are accelerated to such high energies to produce X-ray photons[14]. As a result, the emitted spectrum would show a high energy cut off (E_c) at an energy related to γ_{max} and lower than the X-ray band. As in the PLCool model (with free parameters: B, p and normalisation), this model is characterised by the cooling break E_{br}, linked to the strength of the magnetic field, plus a cut-off at high-energy E_c (induced by γ_{max}).

We assumed an exponential shape above the cut off energy. We noted that such shape is constrained only by the IR2 spectrum and it appears steeper ($\Gamma_X = 3.2 \pm 0.4$) than the simultaneous and cooled NIR slope (see Tab. 6). Therefore any high energy slope steeper than $\Gamma_X \sim 3$ could reproduce the data. We point out that either an exponential or sub-exponential slope can equally fit the data. We also note that most likely the electron distribution will not cut abruptly at γ_{max}, therefore it is expected that the cut off will be further broadened. Despite we could not constrain whether the break is broad, we fixed the shape of the high energy cut off such that the e-folding energy of the exponential cut off is equal to the cut off energy.

The PLCoolEv model provides an excellent representation of the multi-wavelength spectrum at all times during the flare (see Tab. 6 and Fig. 7). It produces either superior fits compared to PLCool model (in particular for IR2), or of comparable statistical quality to the BPL parametrisation and it is physically motivated.

Figure 8 shows the confidence contours projected over the E_{br} versus Γ_{NIR} plane for the PLCoolEv model. The high-energy cut-off is constrained to be at $7 \times 10^{-4} < E_c < 1$ keV in the IR1 spectrum, before the start of the X-ray flare (not shown in Fig. 8). In the PLCool model, the steep photon index observed in X-ray during IR2 is the result of the evolution of the high energy cut-off, which at that time was detected in the X-ray band at $E_c = 3.5^{+0.3}_{-1.1}$ keV. As a consequence of this, the cooling break is not pegged anymore at $E_{br} = 0.6$ eV, instead it spans a larger range of reasonable cooling break energies. Additionally, a flatter NIR slope is allowed. During IR3, IR4 and the mean spectrum, the high energy cut-off was at energies higher than the observed X-ray band ($E_c \gg 10$ keV), consistent with the assumptions of the PLCool model (indeed, we obtained similar results). According to the PLCoolEv model, during the early phase of VB3, the high energy cut-off was evolving and it was located between the NIR and X-ray band. It was caught within the X-ray band during IR2 and it was at very high energy at the X-ray peak (and during IR4).

5.8.1 *Evolution of the magnetic field (assuming a constant escape time)*

In this section we interpret the derived evolution of the energy of the cooling break, as being uniquely due to the variation of the magnetic field of the source (e.g., assuming no variation of the escape time).

Figure 9 shows the light curve of the evolution of the magnetic field intensity during the flare. The flat NIR slope observed at all times indicated that the break has to be, at higher frequency compared to the *SINFONI* band, corresponding to $B < 36$ G. In particular, during IR2 the cooling break is observed at $E_{br} = 1^{+2}_{-0.5}$ eV, corresponding to $B = 30 \pm 8$ G. The values derived by fitting the IR1 spectrum are consistent with this value, however the degeneracy between the energy of the cooling break and of the high energy cut-off led to large uncertainties on the magnetic field strength. We note that a value of $B = 30 \pm 8$ G is fully consistent with the magnetic field present within the central ten Schwarzschild radii and generating the steady emission of Sgr A*. During IR3, close to the peak of the X-ray flare, the magnetic field is observed to be $B = 4.8 \pm 1.7$ G. Interestingly, the magnetic field varied by a factor of > 6 in less than ~ 650 s. During IR4, we assumed that the cut off is located at energies higher than the X-ray band (indeed no evidence for a cut off at or below the X-ray band is observed). Under this assumption[15], we observe that after the X-ray peak and towards the end of the X-ray flare, the magnetic field was measured to rise again to values $B = 14.3^{+12.3}_{-7.0}$ G. The red point in Fig. 9 shows the magnetic field strength derived from the fit of the mean spectrum of VB3. As expected, the average magnetic field value

[14] Assuming that all emission is radiated at 0.29 times the critical frequency, it follows that: $\nu_c \sim 2.5 \times 10^{19}$ Hz $(\gamma_{max}/10^6)^2$ $(B/20$ G) (Longair 2011, equation 8.127), where ν_c is the frequency associated to the high energy cut off.

[15] Would, during IR4, the cut off be located in the X-ray band or below, then the current constraints on the energy of the cooling break should be considered only as upper limits. If this is indeed the case during IR4, then weaker magnetic fields would be allowed and the data point in Fig. 9 should be considered as an upper limit.

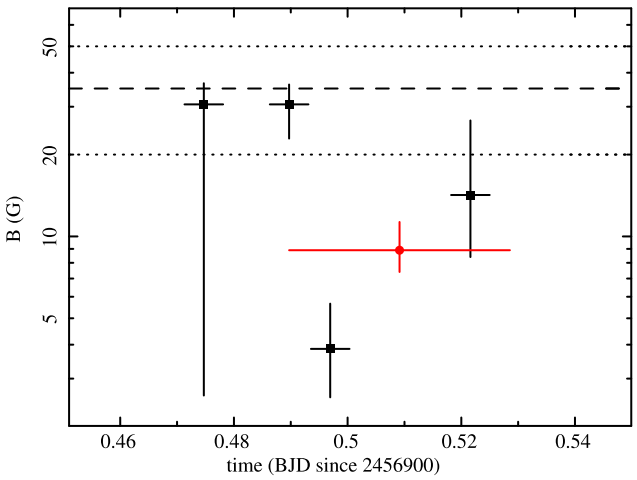

Figure 9. Evolution of the strength of the magnetic field (in Gauss) during and after the flare VB3, in the PLCoolEv model. The black square show the magnetic field strength during IR1 to IR4. The red circle shows the measurement of the average magnetic field during the entire duration of the X-ray flare VB3 (under the assumption of a constant escape time of $t_{esc} = 300$ s). The dotted lines indicate the typical range of magnetic field strengths during quiescence ($B \sim 20 - 50$ G). The dashed line shows the magnetic field strength ($B \sim 36$ G) corresponding to a cooling break within the narrow *SINFONI* band. The flat NIR slopes observed at all times during the flare suggest $B < 36$ G, while the steep NIR slope observed after the VB3 flare (during IR5, IR6 and IR7) suggest $B > 36$ G. The error bars correspond to the 1-sigma uncertainties as derived from the confidence contours shown in Fig. 8. No evidence for a cut off at or below the X-ray band is observed during IR4, therefore the associated measurement is valid under the assumption that the cut off is at energies higher then the X-ray band. Would this assumption be invalid, such constraint should be considered as a upper limit.

during the flare ($B = 8.8^{+5.0}_{-3.0}$ G) was intermediate between IR2, IR3 and IR4 and it was significantly smaller than the one derived during quiescence.

5.8.2 *Evolution of the escape velocity (constant magnetic field)*

The results obtained in section 5.8.1 are valid under the assumption that the synchrotron escape time is constant over the entire duration of the flare. However, it is not a priori set that the escape time has to remain constant over time. Therefore, we now investigate the hypothesis that the escape time evolves, while assuming a constant magnetic field ($B = 30$ G). If so, the energies of the break frequencies observed during IR2, IR3 and IR4 ($E_{br} = 1^{+2}_{-0.5}$, 250^{+780}_{-150} and $9.8^{+77}_{-8.3}$ eV) correspond to an escape velocity of $t_{esc1} = 310 \pm 130$ s, $t_{esc2} = 20 \pm 10$ s and $t_{esc3} = 100^{+150}_{-70}$ s. Therefore, the escape time would drop by a factor of ~ 16 in ~ 600 s, to then increase again.

The escape time is likely related to the source size and/or to the position of the source onto the accretion disc. For example, Dodds-Eden et al. (2009) assume that the escape time is comparable to the dynamical time at a given radius in an accretion disc (t_{dyn}): $t_{esc} \sim t_{dyn} = \sqrt{R^3/2GM_{BH}}$, where R is the source position within the accretion disc, G is the gravitational constant and M_{BH} is the black hole mass. We note that, under this assumption, the escape time assumed throughout the paper ($t_{esc} = 300$ s) corresponds to a reasonable radial position of ~ 3.5 R_S from the BH.

In summary, the PLCoolEv can adequately fit not only the mean properties of the VB3 flare but also its evolution. The major weaknesses of the PLCool model are solved by allowing the high energy cut-off (γ_{max}) to evolve during the flare.

We note that the evolution of the cooling break appears more likely induced by a variation of the magnetic field that drops its intensity by discharging magnetic energy density into particle acceleration and then rises again to its average value, compared to a variation of the escape velocity. Indeed, in the latter scenario it would naively be expected that the energy release produced by the source would make the source size expand with time, instead of contracting. However, we point out that these considerations are not conclusive. Indeed, because of the limitations of our simplified single zone models, we can not discriminate between a pure magnetic field evolution or a pure escape time evolution (or a combination of both).

6 EMISSION AFTER VB3 (X-RAY QUIESCENCE)

IR5 and IR6 have been accumulated after the end of VB3 when only upper limits are observed in X-rays and the NIR flux ($F_{2.2\mu m} \leqslant 4.5$ mJy) corresponds to the faintest fluxes of Sgr A*, detected so far (e.g. Dodds-Eden et al. 2010). These time intervals appear similar to classical quiescent periods. During IR7 a re-brightening is observed in NIR, associated with a hint for an excess in the X-ray band (Fig. 5). Though the NIR flux is relatively high ($F_{2.2\mu m} \sim 7$ mJy), the NIR spectral slope appears steeper than during the flare and fully consistent with the value observed during NIR quiescence. The sparse NIR light curve as well as the low significance of the X-ray excess do not allow us to clarify whether the emission during IR7 is produced by a faint flare, with associated feeble X-ray emission or it is just a NIR fluctuation characteristic of a red noise process, commonly occurring during X-ray quiescence.

We observed that the NIR spectra steepened ~ 15 min after the end of the X-ray flare (see Tab. 3). The steepening was so large ($\Delta\Gamma_{NIR} \sim 1 - 2$) that in all cases (from IR5 to IR7) the extrapolation of the steep power-law observed in the *SINFONI* band (Tab. 3) was consistent with the X-ray upper limits. Figure 6 shows that at medium-high NIR fluxes ($F_{2.2\,\mu m} > 7$ mJy) the photon index is consistent with a constant value of $\Gamma_{NIR} = 1.6$. This implies an electron distribution index of $p \sim 2.2$. We note that in the PLCool (and PLCoolEv) model, as long as $B > 35 - 40$ G, the cooling break would move to frequencies lower than the *SINFONI* band, inducing a steepening of the observed photon index by $\Delta\Gamma_{NIR} = 0.5$. However, this steepening appears too small to reproduce the full extent of the observed photon index variation. We remind the reader that accurate photon index determination at low NIR fluxes are challenging. Therefore, we leave to future dedicated studies to establish the full extent and the reliability of the NIR spectral steepening at low NIR fluxes. If future data confirms the presence of such steep NIR slopes after very bright flares, then this radiation might be associated with thermal Synchrotron emission from electrons transiently heated during VB3. Indeed, we note that, for a magnetic field strength of $B \sim 30$ G, the cooling time of NIR synchrotron electrons is of the order of ~ 500 s, shorter, but comparable, to the time interval between the end of IR4 and the start of IR5 (see Fig. 5 and Tab. 3).

7 DOES A SLOW EVOLVUTION OF γ_{MAX} AGREE WITH THE EVOLUTION OF BRIGHT X-RAY FLARES?

The detailed investigation of the X-ray and NIR emission during VB3 indicates the PLCoolEv as the favourite model (see §5 and 6). The essential component that distinguish the PLCoolEv model from the simpler PLCool model is the evolution of the cut-off (γ_{max}). In particular, we suggest that the evolution of γ_{max} might be relatively slow, spanning the range from optical-NIR to X-rays and beyond on macroscopic time-scales ($\sim 10^2 - 10^3$ s). We also note that the X-ray band has significant extensions in frequency, spanning over a decade in frequency. Therefore, should the PLCoolEv model be correct and should the behaviour observed during the very bright flare VB3 be universal, then this model would predict an energy dependent evolution of X-ray flares that might be tested with archival data of other bright X-ray flares.

Indeed, it is expected that the passage of the cut-off (induced by γ_{max}) through the X-ray band would induce slightly shorter flares at higher energies as well as steeper spectral slopes at the start and end of the X-ray flare. Clearly the full extent of these effects can not be predicted, because it depends on how rapidly the cut-off spans the X-ray band, but we investigated whether we can exclude that such evolution is present during bright X-ray flares. Indeed, despite the fact that at present there are only few bright and very bright flares with multi-wavelength coverage and only one (VB3) with simultaneous NIR and X-ray spectra, the *XMM-Newton* archive contains several bright flares suitable for studying the spectral evolution in the X-ray band[16].

7.1 Time dependence of X-ray spectra of very bright flares

To follow the evolution of Sgr A*'s X-ray emission during very bright X-ray flares, we consider here all bright and very bright flares observed by *XMM-Newton* (see Tab. 1; Ponti et al. 2015a). For each of these flares we extract three spectra, one during the rise, one at the peak and one during the decay (see Tab. 1)[17]. We fit the spectra from both the EPIC-pn and MOS data during the peak of VB1, VB2 and VB3 with the absorbed power-law model. The observed spectral indices at peak are consistent between the different flares; therefore we assume the same value and redo the fit to obtain a best fit value of $\Gamma = 2.08 \pm 0.11$ (± 0.07 at 1 σ). We then repeat this exercise fitting the spectra during both the flare rise and decay, obtaining $\Gamma = 2.33 \pm 0.23$ and $\Gamma = 2.45 \pm 0.25$, respectively. Again, we observe consistent values for the rises and decays of different flares. Therefore we assume the same spectral index during both flanks of the flares, obtaining a best fit value of $\Gamma = 2.36 \pm 0.15$ (± 0.09 at 1 σ), slightly steeper ($\sim 2.4\sigma$ significance) than the spectral index observed at peak. We conclude that the spectra of very bright flares provide hints for (or at least are not in disagreement with) an evolution of the order of $\Delta\Gamma \sim 0.3$ between the peak and the flanks of the flares. This behaviour is reminiscent of what was observed during the evolution of VB3. Indeed, during the early phases of the X-ray emission (IR2), the X-ray spectrum was steeper than at the peak of the X-ray emission (IR3; §5), most likely because of the evolution of γ_{max}.

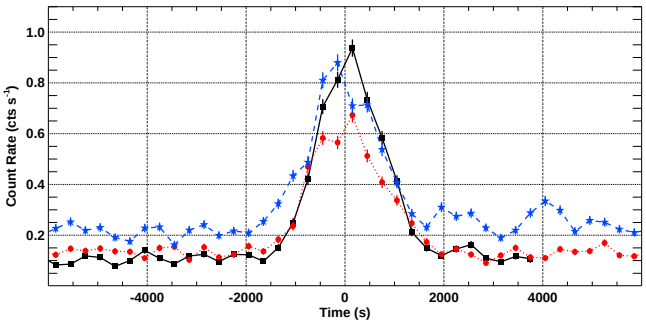

Figure 10. Light curves, in the 2-10 keV band, of the three brightest *XMM-Newton* flares, VB1, VB2 and VB3 are shown with back squares, red circles and blue stars, respectively. The light curves of the three very bright flares observed by *XMM-Newton* show very similar time evolution and comparable duration. These light curves are the result of the sum of the data from EPIC-pn and MOS. For display purposes, we shifted the time axis aligning the peak of the Gaussian best fitting the flare profile (see Tab. 7).

7.2 Colour dependence of bright X-ray flares

Figure 10 shows the 2-10 keV band light curves of the three very bright flares observed by *XMM-Newton* (Ponti et al. 2015a). We combined the light curves from the three EPIC cameras. Figure 10 shows a remarkable similarity in the evolution of these flares, suggesting an analogous origin. We fit each of the light curves with a model composed by a constant plus a Gaussian profile (to fit the flare)[18].

To investigate possible dependences of the X-ray flares on energy, we extracted the X-ray light curves of the three very bright *XMM-Newton* flares in the 2-4, 4-6 and 6-10 keV energy bands. For each flare, we fit the light curves with a constant plus a Gaussian profile, to characterise the flare shape (see Table 7).

The top and bottom panels of Fig. 11 show the best fit flare duration ($FWHM$) and delay as a function of energy. For each energy we report with black squares, red circles and blue stars the values obtained for the flares VB1, VB2 and VB3, respectively. In particular, we show the width of the best fit Gaussians as a proxy for the flare duration and the delay is defined as the peak time of the Gaussian at a given energy minus the peak time in the 4-6 keV band.

The top panel of Fig. 11 suggests that Sgr A*'s flares shorten with energy, typically lasting $\sim$ 5 % less time in the hard band (6-10 keV) compared to the soft one (2-4 keV). The top panel of Fig. 12 shows the combination of all three very bright flares. With the solid red, dotted orange and dashed blue lines the light curves in the 2-4 keV, 4-6 keV and 6-10 keV energy bands are shown. The light curves are shifted by the center of their best-fit Gaussian profile, subtracted by the best-fit local underlying continuum, and normalised by the peak of their best-fit Gaussian (see Tab. 7). The flare profile is tighter at higher energies (Fig. 12, Tab. 7). Indeed,

[16] We do not consider bright flares detected by *Chandra*, because the vast majority of those are affected by strong pile-up, significantly distorting the spectral shape.

[17] For flares VB1 and VB2 we chose three intervals of equal duration, while for flare VB3, the extraction of the spectra during flare rise, peak and decay are chosen in order to optimise the coverage of the *SINFONI* spectra (see Tab. 1, 3 and Fig. 5).

[18] The variation of the non-flare emission during both observations taken on 2007-04-03 and 2014-08-31 was produced by the contribution from the magnetar SGR J1745-2900 (at the level of $\sim$ 50 % to the total observed quiescent flux on 2014-08-30; see also Ponti et al. 2015a) and from the very bright source AX J1745.6-2901 (Ponti et al. 2015b).

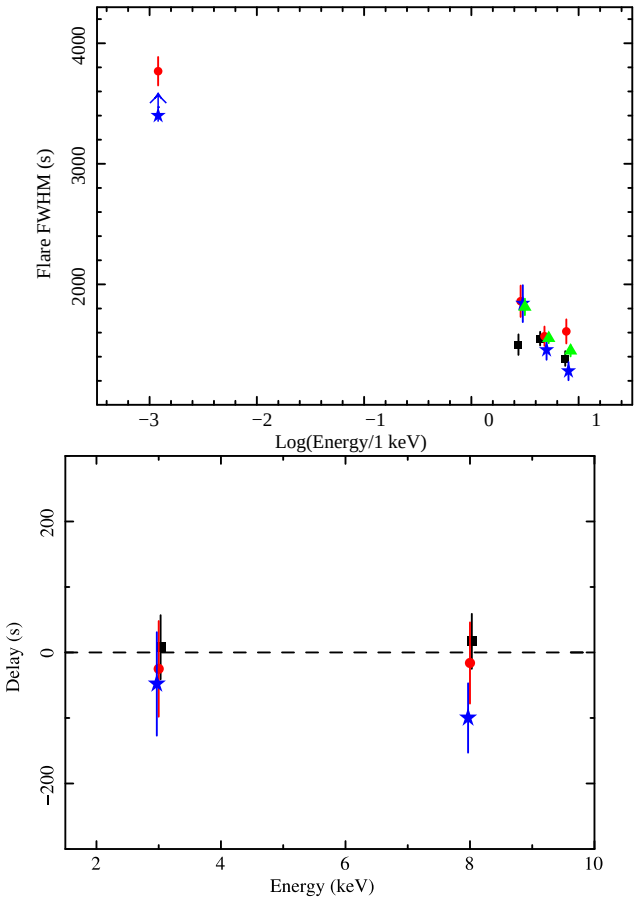

Figure 11. *(Top panel)* Flare duration (FWHM) at various energies of the three brightest *XMM-Newton* flares, VB1, VB2, VB3 and of the combined *XMM-Newton* flare light curve are shown with back squares, red circles, blue stars and green triangles, respectively. The flare duration are computed in the 2-4, 4-6 and 6-10 keV energy bands (the points are slightly shifted for display purposes). Flares are typically shorter at higher energies. We also show the duration of VB2 (as observed in the L' band, see §5.2) and the lower limit on the duration of VB3 (as observed with *SINFONI*). The flare durations in the NIR band connect with the extension of the trend observed in X-rays. *(Bottom panel)* Peak occurrence delay, between different energies (same energy bands as above) for the three very bright flares observed by *XMM-Newton*. The delays are computed as the best fit peak value of the Gaussian at each energy minus the same value observed in the 4-6 keV band. Colour code as before.

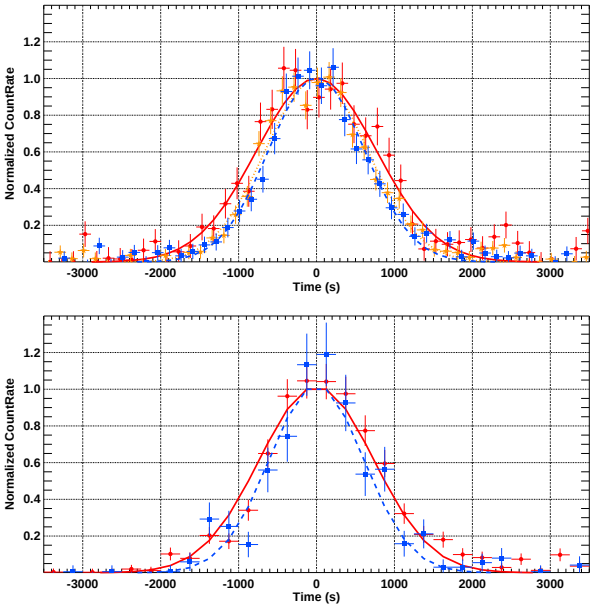

Figure 12. *(Upper panel)* The combination of the light curves of VB1, VB2 and VB3 in the 2-4 keV (red squares), 4-6 keV (orange stars), 6-10 keV (blue squares), light curves are shifted by the center of their best-fit Gaussian profile, subtracted by the best-fit local underlying continuum, and normalised by the peak of their best-fit Gaussian. Time bins of 150 s are used. Flares are shorter in the hard band. *(Bottom panel)* Chandra composite light curve for 2-4.5 keV (red circles) and 6-9 keV (blue squares). All bright flares not significantly affected by pile-up (peak count rate < 0.1 ph s^{-1}) are considered here. The light curves are shifted with the same method described above. Time bins of 250 s are used. Flares last longer in the soft band.

the width of the Gaussian fitting the 6-10 keV band appears to be significantly smaller (at $\sim 4.4\sigma$ significance) by $\sim$ 360 s compared to the 2-4 keV band one (see Tab. 7). To test whether this is a common property of all X-ray flares or whether it is a peculiarity of very bright flares, we combined all *Chandra* bright and very bright flares (i.e. with fluence larger than 5×10^{-9} erg cm^{-2}; see Ponti et al. 2015a for the definition). To avoid flares significantly affected by pile up, we excluded the ones observed in either ACIS-I or ACIS-S with no subarray mode and reaching a block count rate equal or higher than 0.1 ph s^{-1} (see Ponti et al. 2015a for details). We also excluded the flares observed in ACIS-S 1/8 subarray mode and reaching a block count rate equal or higher than 0.8 ph s^{-1} (Ponti et al. 2015a). The bottom panel of Fig. 12 shows the combined *Chandra* flare light curve in the 2-4.5 and 6-9 keV energy bands with red circles and blue squares, respectively. We find that bright *Chandra* flares also last longer in the soft energy band compared to the hard one, with a difference in $FWHM$ of $\sim$ 300 s (Fig. 12 and Tab. 7).

No significant time shift with energy is apparent, with upper limits as tight as $\sim 100 - 200$ s (see bottom panel of Fig. 11).

We conclude that, at present, the X-ray data of the bright flares are not in contradiction with a slow variation of γ_{max}.

8 DISCUSSION

Simultaneous *XMM-Newton*, *NuSTAR* and *SINFONI* observations of Sgr A* allowed us to determine, for the first time, the spectral shape and the evolution of the radiation of a very bright flare. This enabled us to pin down the radiative mechanism during bright flares of Sgr A* and its evolution during the flare. We can rule out that a simple power-law model, representing plain Synchrotron emission, can reproduce the flare emission.

8.1 TSSC

A TSSC model provides an acceptable fit to the data, from a statistical point of view. However: i) the fit is worse than the PLCool and PLCoolEv models, despite the larger number of free parameters; ii) in this framework the observed spectral steepening ($\Delta\Gamma = 0.57 \pm 0.09$ at 1 σ) between NIR and X-ray would be just a coincidence, moreover; iii) the best fit parameters appear implausible.

Indeed, the best fit magnetic field appears unreasonably high ($B \sim 10^4$), the source size unphysically small ($R_F \sim 10^{-2} - 10^{-4}$ R$_S$) and the required source density about seven orders of

Table 7. Results of single Gaussian fitting to the 200 second binned flare light curves without background subtraction, but with `epiclccorr` applied. Note that using the background subtracted light curves only changes these values very slightly. [1]best-fit local continuum under the flare. [2]delay time related to the 4-6 keV band. The errors are all 1 σ. The composite flare from *XMM-Newton* is the combination of VB1, VB2 and VB3. The composite flare from *Chandra* is the combination of a set of unpiled-up flares observed by *Chandra*.

Flare ID	Band *keV*	Contiuum[1] $cts\ s^{-1}$	$FWHM$ *s*	Delay[2] *s*
VB1	2 - 4	0.0446 ± 0.0017	1500 ± 85	$+8 \pm 49$
	4 - 6	0.0310 ± 0.0014	1550 ± 57	0
	6 - 10	0.0128 ± 0.0009	1385 ± 61	$+17 \pm 42$
VB2	2 - 4	0.0485 ± 0.0008	1860 ± 130	-25 ± 73
	4 - 6	0.0433 ± 0.0008	1570 ± 80	0
	6 - 10	0.0198 ± 0.0005	1610 ± 100	-16 ± 62
VB3	2 - 4	0.0956 ± 0.0016	1840 ± 153	-48 ± 79
	4 - 6	0.0893 ± 0.0015	1455 ± 80	0
	6 - 10	0.0273 ± 0.0008	1280 ± 75	-100 ± 53
Composite (XMM)	2 - 4	0.0610 ± 0.0007	1813 ± 68	–
	4 - 6	0.0559 ± 0.0007	1554 ± 42	–
	6 - 10	0.0242 ± 0.0004	1450 ± 47	–
Composite (*Chandra*)	2 - 4.5	$7.9 \pm 0.3 \times 10^{-4}$	1730 ± 56	–
	4.5 - 6	$4.1 \pm 0.2 \times 10^{-4}$	1693 ± 59	–
	6 - 9	$6.0 \pm 0.4 \times 10^{-4}$	1424 ± 89	–

magnitude higher than what is estimated to be present in the accretion flow around Sgr A* (Loeb & Waxman 2007; Genzel et al. 2010). As discussed in Dodds-Eden et al. (2009), these unreasonable best fit parameters are consequences of the assumptions intrinsic to the TSSC model considered here. In particular, to fit the soft X-ray emission via inverse Compton up-scattering of NIR or sub-mm radiation, the energies of the electrons involved in the flare is restricted to be lower than $\gamma_e < 100$. On the other hand the requirement of the observed hard NIR slope constrains the magnetic field to be larger than $B > 10^3$ G. Finally, the ratio of the synchrotron to inverse Compton luminosity requires that the size of the source has to be $R_F < 10^{-2}\ R_S$. Therefore, it appears that this simplistic TSSC model, cannot adequately explain the flare emission.

The observed spectral steepening ($\Delta\Gamma = 0.57 \pm 0.09$, 1 σ) between NIR and X-rays of the mean spectrum suggests that the radiative process during bright flares might be synchrotron radiation with a cooling break. Therefore, we explored in more details this scenario, instead of considering more complex synchrotron self Compton (SSC) models. Nonetheless, this does not rule out that more complex TSSC and non-thermal SSC models might be invoked to explain the X-ray radiation.

8.2 PLCool

We observed that the synchrotron model with a cooling break can reproduce both the mean spectrum and the evolution of the SED of Sgr A* during the entire duration of a very bright flare (apart from IR2). In particular, the observed spectral steepening of both the mean spectrum and of the emission at the X-ray peak (IR3) is a strong indication that synchrotron with cooling break might be the dominant radiative mechanism. In this simplistic model, the "unknown" motor powers the continuous acceleration of energetic electrons with a power-law distribution. An important difference of the PLCool model compared to the TSSC model, is that the motor is assumed to accelerate electrons into a power-law distribution up to $\gamma_{max} \geqslant 10^6$, therefore the synchrotron radiation is not limited to the NIR band, instead it extends to X-ray and higher energies.

Limitations of the model

We point out that, for simplicity, we reproduce the synchrotron emission with a simple broken power law model. We note that the cooling break typically occurs in the unobserved optical-UV band, therefore we can not currently constrain whether the cooling break is a sharp feature or it is significantly extended in energy. Indeed, we do not observe any significant curvature in either the NIR or X-ray band, however this has to be attributed to the small frequency windows sampled by our data. Therefore, for simplicity, we assume a sharp break, though realistic synchrotron models can be significantly broadened (by up to more than a decade in energy; Dibi et al. 2014). Indeed, it is beyond the scope of this paper to employ more complex synchrotron models. We also note that significantly different statistics characterise the time resolved spectra in the NIR and X-ray bands. Therefore, the broad band fit of the time resolved spectra are primarily driven by the NIR photon index. It is important to point out that at the beginning of the flare, the cooling break is observed to be located either within or very close to the NIR band. Therefore, should a broadened break be present at that time, it might potentially affect some of the model parameters. Future investigations will clarify the extent of this.

Difficulties of the PLCool model

As already briefly mentioned in §5.6, we stress again here that the most difficult problem of the PLCool model is related to the best fit energy of the cooling break. Indeed, both for IR1 and IR2 the break is observed within the NIR band (see Tab. 6). During IR1 this result is driven by the combined upper limit on the X-ray emission and by the high flux and flat photon index in the *SINFONI* band, inducing a cooling break suspiciously located at energies just higher than $\sim$ 0.6 eV, the upper bound of the *SINFONI* spectrum. Similar results holds during IR2. Indeed, at that time, the X-ray flare had already started, alleviating the problem, however the NIR band showed a slightly flatter power-law ($\Gamma_{NIR} = 1.59 \pm 0.2$; Tab. 3), therefore the cooling break was observed to again be placed at the upper bound of the *SINFONI* spectrum (moreover the steep X-ray slope is not completely reproduced). We consider a rather unlikely possibility that, by chance, the cooling break occurred twice within the narrow NIR band.

The biggest pitfall that the PLCool model has to overcome is the explanation of the early phases of the VB3 flare. Indeed, at the basis of the PLCool model there is the assumption that the NIR and X-ray emissions are tied by a broken power law. Therefore, within this framework one would predict that the NIR to X-ray emission are strictly related and they follow each other. The only deviation to this "rule" could be generated by the possible delay of the NIR radiation associated with the longer NIR synchrotron cooling time. Therefore, it is expected that the X-ray emission either rises before or at the same time as the NIR one. One possible way out (that has been considered in the past to explain the delayed X-ray emission in the early phases of the very bright flares) was to assume that the early NIR emission had a very steep slope. However, we can now rule out that this is happening during VB3. Indeed, during IR1 bright NIR emission, with a flat slope ($\Gamma_{NIR} = 1.48 \pm 0.2$;

Tab. 3), is observed at the same time of tight upper limits to the X-ray emission. On the contrary, no prominent X-ray radiation is observed either during or before IR1, with upper limits in the 3-10 keV band of $F_{3-10\ keV} < 2.3 \times 10^{-12}$ erg cm^{-2} s^{-1}.

The third difficulty of the PLCool model is to properly reproduce the IR2 spectrum. A fit with the BPL model shows that the difference of the X-ray to NIR photon index is significantly higher $\Delta\Gamma = 1.8 \pm 0.4$ than the one expected by the cooling break model $\Delta\Gamma = 0.5$ (Tab. 6). This resulted in a poor fit of IR2 by the PLCool model (indeed an F-test suggests that the BPL model provided a significantly better description of the IR2 spectrum, at > 99 % confidence).

8.3 PLCoolEv

We then relaxed the requirement that γ_{max} has to be $> 10^6$ at all times. We postulated that, γ_{max} increases slowly with time (e.g. many times the Alfvén speed crossing time of a source of a size of few Schwarzschild radii), generating a cut-off that gradually moves to higher energies, eventually transiting through the X-ray band and producing a bright X-ray radiation with a delay compared to the start of the NIR flare. Regardless of the behaviour of γ_{max} at the end of the flare, the PLCoolEv (as well as PLCool) model predicts a delay of a few hundred seconds of the NIR radiation, compared to the X-ray emission (§5.8), in agreement with a longer duration of the NIR flare.

Limitations of the model

For simplicity, we assumed an exponential drop of the high energy cut off in the synchrotron spectrum, with a shape such that the e-folding energy is equal to the cut off energy. We note that the high energy cut off is detected in the observed band only once, during IR2. During this interval, the X-ray slope is steeper ($\Gamma = 3.2 \pm 0.4$) than the simultaneous NIR one, however the statistics is not enough to discriminate its detailed shape. For example, we could not distinguish either between an exponential or a sub-exponential, or we could not constrain the broadness of the cut off. Therefore, should a broadened break be present at that time, it might potentially affect some of the model parameters. For instance, broader cutoffs in IR2 and IR4 might allow for a cooling break at higher energy, implying a weaker magnetic field. Future investigations will clarify the extent of this.

8.3.1 Comparison of the PLCoolEv model to the data

The PLCoolEv model provides an excellent description of the mean spectrum of VB3 and of its evolution over time. In fact, it naturally explains the periods during which bright and flat-spectrum NIR radiation is observed, simultaneous with no X-ray emission (e.g. IR1). In particular, the passage of the cut-off within the X-ray band generates: i) shorter flare durations at higher energies; ii) right at the start of the X-ray flare steeper X-ray spectra than expected by the cooling break (e.g. IR2) and; iii) possibly steeper spectra in the flanks of the X-ray flare than at the peak, such as observed.

We also measured a significant evolution of the cooling break during the flare. Under the assumption that the escape time remains constant, this suggests that the strength of the magnetic field (typically of several tens of Gauss) lowers to values of few Gauss during the peak of bright flares, to return to high values after that. For a thermal distribution of electrons with temperature θ_E, the Synchrotron luminosity is proportional to the square of the magnetic field ($L_{Synch} \propto N\theta_E^2 B^2$), therefore the drop of the magnetic field strength at the flare peak would appear contradictory. However, in this scenario, the large Synchrotron luminosity is provided by the vast increase in the energy of the accelerated particles. It is likely that the acceleration mechanism is powered by the magnetic field, that therefore gradually reduces its strength during the flare (Dodds-Eden et al. 2009; 2010; 2011). Indeed, a similar process is at work in magnetic reconnection that is a fundamental process of plasmas in which magnetic energy is converted into particle acceleration through magnetic field rearrangement and relaxation (Begelman 1998; Lyubarski 2005; Zweibel & Yamada 2009; Sironi et al. 2014; 2016). The observed drop of the magnetic field, right at the peak of the flare, is in line with the predictions of magnetic reconnection models.

We conclude that the data are consistent with such an evolution of the magnetic field.

8.3.2 Constraints on energy power and source size

Is the energy stored in the magnetic field enough to power the flare? We estimated the total energy emitted during the VB3 flare by considering that the NIR and X-ray luminosity was at a level of $\sim$ 10 mJy and $\sim 2 \times 10^{35}$ erg s^{-1} for about $\sim 3.8 \times 10^3$ s and $\sim 1.8 \times 10^3$ s, respectively, resulting in a total emitted energy of $\sim 8 \times 10^{38}$ erg. If we discharge the magnetic energy within a spherical region with $\sim 1.5\ R_S$ radius, bringing its magnetic field from $B \sim 30 - 40$ G to ~ 5 G, then about $\sim 8 - 15 \times 10^{38}$ erg are produced. This appears to be enough energy to power the VB3 flare. Moreover, this suggests that the source of VB3 had a size $\geqslant 1.5\ R_S$.

9 CONCLUSIONS

- The mean X-ray photon index during the very bright flare VB3 is significantly steeper ($\Gamma_X = 2.27 \pm 0.12$) than the simultaneous ($\Gamma_{NIR} = 1.7 \pm 0.1$) NIR one, excluding that the radiative process can be described by a simple power-law. In particular, the observed steepening ($\Delta\Gamma = 0.57 \pm 0.09$ at 1 σ) is consistent with what is expected by Synchrotron emission with a cooling break ($\Delta\Gamma = 0.5$).
- We observe bright $F_{2.2\mu m} = 8.9 \pm 0.1$ mJy and hard NIR ($\Gamma_{NIR} = 1.48 \pm 0.23$) emission about $\sim 10^3$ s before the start of the X-ray flare. We also observe very steep X-ray emission ($\Gamma_X = 3.2 \pm 0.4$) at the start of the X-ray flare, while the contemporaneous NIR photon index was $\Gamma_{NIR} = 1.4 \pm 0.2$. These results strongly support a scenario where the synchrotron emitting electron power-law distribution has a cut-off (γ_{max}) that is *slowly* evolving with time, therefore inducing an evolving high energy cut-off in the spectrum.
- The data are consistent with an evolution of the magnetic field strength during the flare (under the assumption of a constant escape time). Large magnetic field amplitudes ($B = 30 \pm 8$ G) are observed at the start of the X-ray flare. The magnetic field strength drops to $B = 4.8 \pm 1.7$ G, at the peak of the X-ray flare, a variation of a factor of > 6 in less than ~ 650 s. It then increases again in the decreasing flank of the flare ($B = 14.3^{+12.3}_{-7.0}$ G). This is consistent with a scenario where the process that accelerates the electrons producing the Synchrotron emission is tapping energy from the magnetic field (such as, e.g. in magnetic reconnection).

• From the total emitted energy and the variation of the magnetic field, we estimated that the source size of the VB3 flare has to be larger than $\geqslant 1.5\ R_S$, if powered by magnetic reconnection.

• We observe hints for steeper, by roughly $\Delta\Gamma = 0.3$, X-ray spectra during the rise and the decay of an X-ray flare, compared to the values at peak. This indicates that, despite the fact that the photon index is similar between different X-ray flares, there might be significant spectral evolution during each X-ray flare. This is an expectation of the PLCoolEv model.

• Bright and very bright *XMM-Newton* and *Chandra* flares typically last significantly ($\sim 4.4\sigma$ significance) longer, by ~ 300 s at soft X-ray energies, compared to harder ones (2-4 and 6-10 keV, respectively). This trend appears to join smoothly to the longer duration typically observed in the NIR band. Again, this is most probably the product of the evolution of γ_{max}.

• The three very bright flares, caught by *XMM-Newton* so far, have very similar light curves and spectral properties, indicating an analogous physical origin. This suggests that the results of this study on VB3 could be universal to bright and very bright flares.

• The best fit column density of neutral absorbing material observed during the X-ray spectra of the very bright flares of Sgr A* is constant and it is consistent with the values observed in nearby sources. Indeed, the three bright transients within $d_{\rm pro} < 1.5'$ from Sgr A* (SGR J1745-2900, Swift J174540.7-290015 and the foreground component towards AX J1745.6-2901) show neutral absorption column densities consistent with the value of Sgr A* (Coti-Zelati et al. 2015; Ponti et al. 2016a; 2016). This suggests that the neutral absorption towards Sgr A* has an ISM origin.

• Synchrotron self Compton models can statistically reproduce the flare emission and its evolution. On the other hand, they imply unrealistic parameters. In such a scenario it would be an unlikely coincidence that the NIR photon index is flatter than the X-ray one by $\Delta\Gamma = 0.5$. Moreover, the evolution of the density, source radius and magnetic field before, during and after the very bright flare appears improbable.

ACKNOWLEDGMENTS

The authors wish to thank Jan-Uwe Ness, Ignacio de la Calle, Karl Foster and the rest of the *XMM-Newton* and *NuSTAR* scheduling teams for the enormous support that made this multi-wavelength campaign possible, as well as the referee for the careful reading of the paper. GP thanks Lorenzo Sironi, Hendrik J. van Eerten, Michi Bauböck and Francesco Coti-Zelati, for useful discussion. RT and AG acknowledge support from CNES. This research has made use both of data obtained with *XMM-Newton*, an ESA science mission with instruments and contributions directly funded by ESA Member States and NASA, and on data obtained from the Chandra Data Archive. The GC *XMM-Newton* monitoring project is supported by the Bundesministerium für Wirtschaft und Technologie/Deutsches Zentrum für Luft- und Raumfahrt (BMWI/DLR, FKZ 50 OR 1408 and FKZ 50 OR 1604) and the Max Planck Society.

APPENDIX A: FURTHER DETAILS ON *XMM-Newton* DATA REDUCTION

All X-ray observations considered here have been accumulated with the EPIC-pn and EPIC-MOS cameras in Full Frame mode with the medium filter applied (apart from ObsID 0111350301 which has the pn camera with the thick filter; see Ponti et al. 2015a,b). Sgr A*'s flares in Tab. 1 occurred during periods of negligible soft proton flare activity, therefore no cut was performed during those flares. On the other hand, significant soft proton flares are detected during quiescent emission. We removed these periods of enhanced background activity by cutting all intervals with more than 0.25 ph s^{-1} in the background light curve (integrated over the 10-15 keV energy band, with 20 s time bins and extracted from a $3'$ radius). We selected only single and double events and we used (FLAG == 0) and either (#XMMEA_EP) or (#XMMEA_EM) for EPIC-pn or MOS, respectively. We applied the SAS task LCCORR to the *XMM-Newton* light curves.

We note that during obsID: 0743630201, 0743630301 and 0743630501 Sgr A*'s flux is contaminated by the X-ray emission from the magnetar SGR J1745-2900, located at only $\sim 2.4''$ from Sgr A* (Degenaar et al. 2013; Mori et al. 2013; Rea et al. 2013). During these observations the magnetar's flux was $F_{1-10\ \rm keV} \sim 3\times10^{-12}$ erg cm^{-2} s^{-1} (see Coti Zelati et al. 2015; for the details of the decay curve), therefore allowing an adequate characterisation of the bright flares.

‡ We report in Tab. 1 the same time systems as used by *XMM-Newton* (see § 6.1.4 in *XMM-Newton* Users Handbook, https:heasarc.gsfc.nasa.govdocsxmmuhbreftime.html). The reference or zero time has been defined as: 1998-01-01T00:00:00.00 TT = 1997-12-31T23:58:56.816 UTC. The conversion from TT to UTC at the reference date is TT = UTC + 63.184 s and can be derived from The Astronomical Almanac for other dates.

APPENDIX B: SPECTRAL DISTORTIONS INTRODUCED BY DUST SCATTERING

As already discussed in §3.1, dust scattering does severely distort the source spectrum and if its effects are not properly taken into account, it could significantly bias the results. To provide the reader with a better understanding of the extent of this effect on the various best fit parameters, we present in Tab. B1 the best fit results of the mean X-ray spectrum of VB3 after the application of: i) no correction; ii) corrections with the DUST model and; iii) correction with the FGCDUST model. For these fits we left the column density of neutral absorbing material free to vary. When we applied the DUST model, we tied the dust scattering optical depth τ to the fitted column density so that $\tau = 0.324(N_H/10^{22}\ cm^{-2})$, following Nowak et al. (2012). We also assumed a ratio of 10 between the size of the halo at 1 keV and the extraction region.

The best fit results in Tab. B1 show that the inclusion of the dust scattering model allows us to recover a steeper and brighter source spectrum. Indeed, the main effect of dust scattering is to remove flux from the line of sight and to spread it in the halo, that

Table B1. Best fit parameters, once the mean X-ray spectrum of VB3 is corrected with different dust scattering models. Column densities are in 10^{23} cm^{-2} units. Fluxes are in 10^{-12} erg s^{-1} cm^{-2} units, integrated over the $3-10$ keV band and are absorbed, but corrected for the effect of dust scattering. The *XMM-Newton* spectrum is fitted with an absorbed power-law modified by the dust scattering.

	No dust	DUST	FGCDUST
N_H	1.8 ± 0.3	1.3 ± 0.2	1.6 ± 0.3
Γ	2.0 ± 0.3	2.1 ± 0.3	2.2 ± 0.3
F_{3-10}	$7.4^{+10.8}_{-3.6}$	$8.3^{+7.2}_{-3.7}$	$8.9^{+9.0}_{-4.4}$
χ^2/dof	$125.8/116$	$124.2/116$	$126.9/116$

is typically partly lost because of the small source extraction region. Moreover, the probability of dust scattering is higher at low energy, producing a deficiency of low energy photons in the observed spectrum (that is generally reproduced by a higher column density of absorbing material and flatter spectra). Therefore, once the correction for dust scattering is introduced, we observe that the flux increases by ~ 20 %, the column density of neutral material is lower and the spectrum steepens. In particular, we observe the photon index to steepen by $\Delta\Gamma \sim 0.2$. It is important to note that different dust models lead to photon indexes that differ by $\Delta\Gamma = 0.1$ (see Tab. B1).

For this reason, we performed again all the analyses in the paper, correcting the effects of dust scattering with the DUST model. The fit of the mean VB3 X-ray spectrum results in a $\Gamma_X = 2.16 \pm 0.14$, that once compared to the NIR slope $\Gamma_{NIR} = 1.7 \pm 0.1$, gives $\Delta\Gamma = 0.46 \pm 0.17$ (± 0.10 at 1 σ), which is completely consistent with the PLCool model ($\Delta\Gamma = 0.5$). The same applies also to the IR3 interval. Indeed, the X-ray photon index during IR3 is $\Gamma_X = 2.5 \pm 0.3$, therefore steeper by $\Delta\Gamma = 0.6 \pm 0.3$, compared to the simultaneous NIR measurement ($\Gamma_{NIR} = 1.9^{+0.1}_{-0.2}$). Therefore, it is in this case also consistent with the conclusions of this work.

The blue, green, and black data in Fig. B1 show the *XMM-Newton* de-absorbed mean spectrum of VB3 (see also Fig. 4) after correcting the observed spectrum for the effects of dust scattering with the FGCDUST, DUST models and after applying no correction, respectively. The blue dotted lines show the uncertainties in the determination of the X-ray slope if no correction for dust scattering is applied. Even in this case, the difference in X-ray and NIR spectral shapes are consistent with the predictions of the synchrotron model with cooling break.

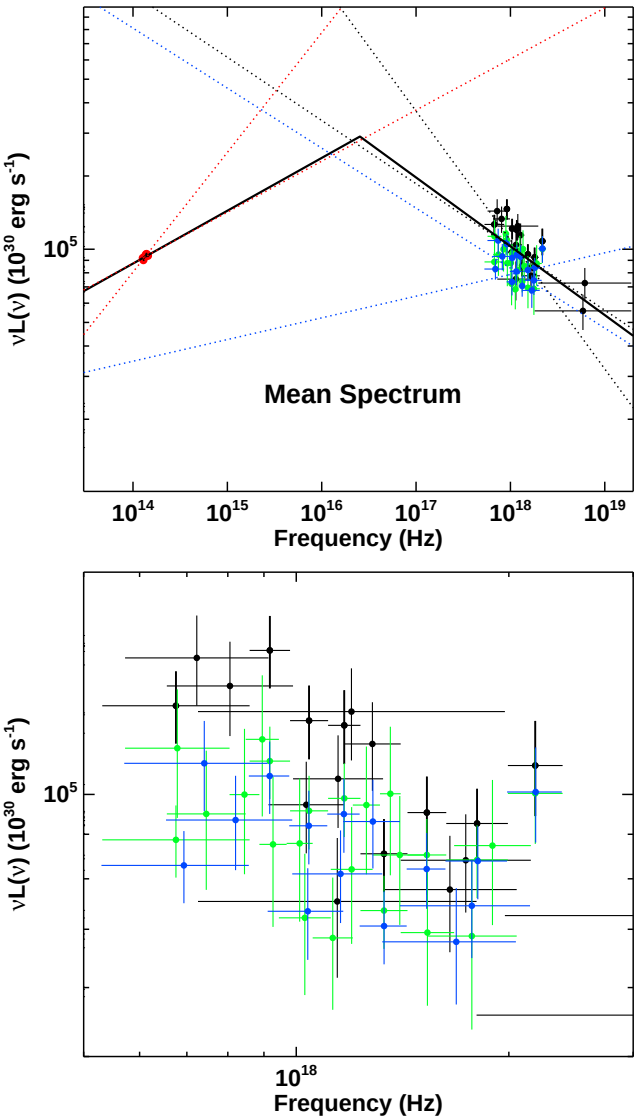

Figure B1. *(Top panel)* The red points show the mean NIR (*SINFONI*) during the VB3 flare, such as in Fig. 4. The blue points show the corresponding X-ray (*XMM-Newton* and *NuSTAR*) spectra, when no dust correction is applied. The green and black points show the X-ray spectra corrected for the effects of dust scattering according to the DUST and FGCDUST models, respectively. The stronger the correction, the brighter and steeper becomes the X-ray spectrum (see text for details). The red, blue and black dotted lines show the uncertainty on the NIR slope, on the X-ray slope when no correction for dust is applied and once the data are corrected using the FCGDUST model, respectively. The black line shows the best fit PLCool model (where the X-ray and NIR slopes are tied). All data and models and data are de-absorbed. *(Bottom panel)* Enlargement of the top panel into the X-ray band, to allow a better elucidation of the extent of the effect.

REFERENCES

An, T., Goss, W. M., Zhao, J.-H., et al. 2005, ApJ, 634, L49
Baganoff, F. K., Bautz, M. W., Brandt, W. N., et al. 2001, Nature, 413, 45
Baganoff, F. K., Maeda, Y., Morris, M., et al. 2003, ApJ, 591, 891
Ball, D., Özel, F., Psaltis, D., & Chan, C.-k. 2016, ApJ, 826, 77
Barrière, N. M., Tomsick, J. A., Baganoff, F. K., et al. 2014, ApJ, 786, 46
Begelman, M. C. 1998, ApJ, 493, 291
Bélanger, G., Goldwurm, A., Melia, F., et al. 2005, ApJ, 635, 1095
Bonnet, H., Abuter, R., Baker, A., et al. 2004, The Messenger, 117, 17
Bower, G. C., Deller, A., Demorest, P., et al. 2014, ApJ, 780, L2
Bower, G. C., Markoff, S., Dexter, J., et al. 2015, ApJ, 802, 69
Brinkerink, C. D., Falcke, H., Law, C. J., et al. 2015, A&A, 576, A41
Bremer, M., Witzel, G., Eckart, A., et al. 2011, A&A, 532, A26
Clénet, Y., Rouan, D., Gratadour, D., et al. 2004, A&A, 424, L21
Coti Zelati, F., Rea, N., Papitto, A., et al. 2015, MNRAS, 449, 2685
Cuadra, J., Nayakshin, S., Springel, V., & Di Matteo, T. 2005, MNRAS, 360, L55
Cuadra, J., Nayakshin, S., Springel, V., & Di Matteo, T. 2006, MNRAS, 366, 358
Cuadra, J., Nayakshin, S., & Martins, F. 2008, MNRAS, 383, 458
Czerny, B., Nikołajuk, M., Piasecki, M., & Kuraszkiewicz, J. 2001, MNRAS, 325, 865
Degenaar, N., Miller, J. M., Kennea, J., et al. 2013, ApJ, 769, 155
Díaz Trigo, M., Parmar, A. N., Boirin, L., Méndez, M., & Kaastra, J. S. 2006, A&A, 445, 179
Dibi, S., Markoff, S., Belmont, R., et al. 2014, MNRAS, 441, 1005
Dibi, S., Markoff, S., Belmont, R., et al. 2016, MNRAS, 461, 552
Do, T., Ghez, A. M., Morris, M. R., et al. 2009, ApJ, 691, 1021
Dexter, J., Kelly, B., Bower, G. C., et al. 2014, MNRAS, 442, 2797
Dodds-Eden, K., Porquet, D., Trap, G., et al. 2009, ApJ, 698, 676
Dodds-Eden, K., Sharma, P., Quataert, E., et al. 2010, ApJ, 725,

450
Dodds-Eden, K., Gillessen, S., Fritz, T. K., et al. 2011, ApJ, 728, 37
Eckart, A., Baganoff, F. K., Morris, M., et al. 2004, A&A, 427, 1
Eckart, A., Baganoff, F. K., Schödel, R., et al. 2006, A&A, 450, 535
Eckart, A., Schödel, R., García-Marín, M., et al. 2008, A&A, 492, 337
Eckart, A., Baganoff, F. K., Morris, M. R., et al. 2009, A&A, 500, 935
Eckart, A., García-Marín, M., Vogel, S. N., et al. 2012, A&A, 537, A52
Eisenhauer, F., Abuter, R., Bickert, K., et al. 2003, Proc. SPIE, 4841, 1548
Eisenhauer, F., Genzel, R., Alexander, T., et al. 2005, ApJ, 628, 246
Falcke, H., Goss, W. M., Matsuo, H., et al. 1998, ApJ, 499, 731
Fritz, T. K., Gillessen, S., Dodds-Eden, K., et al. 2011, ApJ, 737, 73
Genzel, R., Schödel, R., Ott, T., et al. 2003, Nature, 425, 934
Genzel, R., Eisenhauer, F., & Gillessen, S. 2010, Reviews of Modern Physics, 82, 3121
Ghez, A. M., Wright, S. A., Matthews, K., et al. 2004, ApJ, 601, L159
Gierliński, M., Nikołajuk, M., & Czerny, B. 2008, MNRAS, 383, 741
Gillessen, S., Eisenhauer, F., Quataert, E., et al. 2006, ApJ, 640, L163
Goldwurm, A., Brion, E., Goldoni, P., et al. 2003, ApJ, 584, 751
Haubois, X., Dodds-Eden, K., Weiss, A., et al. 2012, A&A, 540, A41
Helder, E. A., Vink, J., Bykov, A. M., et al. 2012, SSRv, 173, 369
Herrnstein, R. M., Zhao, J.-H., Bower, G. C., & Goss, W. M. 2004, AJ, 127, 3399
Hora, J. L., Witzel, G., Ashby, M. L. N., et al. 2014, ApJ, 793, 120
Hornstein, S. D., Matthews, K., Ghez, A. M., et al. 2007, ApJ, 667, 900
Kardashev, N. S. 1962, SOVAST, 6, 317
Kennea, J. A., Krimm, H., Barthelmy, S., et al. 2013, The Astronomer's Telegram, 5009,
Lagage, P. O., & Cesarsky, C. J. 1983, A&A, 125, 249
Liu, S., Petrosian, V., & Melia, F. 2004, ApJ, 611, L101
Liu, S., Melia, F., & Petrosian, V. 2006, ApJ, 636, 798
Loeb, A., & Waxman, E. 2007, JCAP, 3, 011
Liu, H. B., Wright, M. C. H., Zhao, J.-H., et al. 2016, arXiv:1604.00599
Lyubarsky, Y. E. 2005, MNRAS, 358, 113
Markoff, S., Falcke, H., Yuan, F., & Biermann, P. L. 2001, A&A, 379, L13
Marrone, D. P., Moran, J. M., Zhao, J.-H., & Rao, R. 2006, ApJ, 640, 308
Marrone, D. P., Moran, J. M., Zhao, J.-H., & Rao, R. 2007, ApJ, 654, L57
Marrone, D. P., Baganoff, F. K., Morris, M. R., et al. 2008, ApJ, 682, 373-383
Melia, F. 1992, ApJ, 387, L25
Meyer, L., Eckart, A., Schödel, R., et al. 2006, A&A, 460, 15
Meyer, L., Schödel, R., Eckart, A., et al. 2007, A&A, 473, 707
Meyer, L., Do, T., Ghez, A., et al. 2008, ApJ, 688, L17
Meyer, L., Do, T., Ghez, A., et al. 2009, ApJ, 694, L87
Mori, K., Gotthelf, E. V., Barriere, N. M., et al. 2013, The Astronomer's Telegram, 5020,
Mori, K., Gotthelf, E. V., Zhang, S., et al. 2013, ApJ, 770, L23
Mościbrodzka, M., Gammie, C. F., Dolence, J. C., Shiokawa, H., & Leung, P. K. 2009, ApJ, 706, 497
Mościbrodzka, M., & Falcke, H. 2013, A&A, 559, L3
Mościbrodzka, M., Falcke, H., Shiokawa, H., & Gammie, C. F. 2014, A&A, 570, A7
Mossoux, E., Grosso, N., Vincent, F. H., & Porquet, D. 2015, A&A, 573, A46
Narayan, R., Mahadevan, R., Grindlay, J. E., Popham, R. G., & Gammie, C. 1998, ApJ, 492, 554
Neilsen, J., Nowak, M. A., Gammie, C., et al. 2013, ApJ, 774, 42
Neilsen, J., Markoff, S., Nowak, M. A., et al. 2015, ApJ, 799, 199
Nishiyama, S., Tamura, M., Hatano, H., et al. 2009, ApJ, 702, L56
Nowak, M. A., Neilsen, J., Markoff, S. B., et al. 2012, ApJ, 759, 95
Özel, F., Psaltis, D., & Narayan, R. 2000, ApJ, 541, 234
Pacholczyk, A. G. 1970, Series of Books in Astronomy and Astrophysics, San Francisco: Freeman, 1970,
Parizot, E., Marcowith, A., Ballet, J., & Gallant, Y. A. 2006, A&A, 453, 387
Petrosian, V., & Liu, S. 2004, ApJ, 610, 550
Ponti, G., Fender, R. P., Begelman, M. C., et al. 2012b, MNRAS, 422, 11
Ponti, G., Papadakis, I., Bianchi, S., et al. 2012, A&A, 542, A83
Ponti, G., Morris, M. R., Terrier, R., & Goldwurm, A. 2013, Cosmic Rays in Star-Forming Environments, 34, 331
Ponti, G., De Marco, B., Morris, M. R., et al. 2015a, MNRAS, 454, 1525
Ponti, G., Bianchi, S., Muñoz-Darias, T., et al. 2015b, MNRAS, 446, 1536
Ponti, G., Morris, M. R., Terrier, R., et al. 2015c, MNRAS, 453, 172
Ponti, G., Jin, C., De Marco, B., et al. 2016a, MNRAS, 461, 2688
Ponti, G., Bianchi, S., Muñoz-Darias, T., et al. 2016b, Astronomische Nachrichten, 337, 512
Porquet, D., Predehl, P., Aschenbach, B., et al. 2003, A&A, 407, L17
Porquet, D., Grosso, N., Predehl, P., et al. 2008, A&A, 488, 549
Predehl, P., & Schmitt, J. H. M. M. 1995, A&A, 293,
Quataert, E. 2002, ApJ, 575, 855
Rea, N., Esposito, P., Pons, J. A., et al. 2013, ApJ, 775, L34
Reid, M. J., Menten, K. M., Zheng, X. W., et al. 2009, ApJ, 700, 137-148
Reynolds, M., Kennea, J., Degenaar, N., Wijnands, R., & Miller, J. 2016, The Astronomer's Telegram, 8649,
Roy, S. 2013, ApJ, 773, 67
Schödel, R., Eckart, A., Mužić, K., et al. 2007, A&A, 462, L1
Schödel, R., Najarro, F., Muzic, K., & Eckart, A. 2010, A&A, 511, A18
Schödel, R., Morris, M. R., Muzic, K., et al. 2011, A&A, 532, A83
Sironi, L., & Spitkovsky, A. 2014, ApJ, 783, L21
Sironi, L., Giannios, D., & Petropoulou, M. 2016, MNRAS, 462, 48
Smith, R. K., Valencic, L. A., & Corrales, L. 2016, ApJ, 818, 143
Stone, J. M., Marrone, D. P., Dowell, C. D., et al. 2016, ApJ, 825, 32
Trap, G., Goldwurm, A., Terrier, R., et al. 2010, Advances in Space Research, 45, 507
Trap, G., Goldwurm, A., Dodds-Eden, K., et al. 2011, A&A, 528, A140
Trippe, S., Paumard, T., Ott, T., et al. 2007, MNRAS, 375, 764

Verner, D. A., Ferland, G. J., Korista, K. T., & Yakovlev, D. G. 1996, ApJ, 465, 487
Werner, G. R., Uzdensky, D. A., Begelman, M. C., Cerutti, B., & Nalewajko, K. 2016, arXiv:1612.04493
Wilms, J., Allen, A., & McCray, R. 2000, ApJ, 542, 914
Witzel, G., Eckart, A., Bremer, M., et al. 2012, ApJS, 203, 18
Witzel, G., Morris, M., Ghez, A., et al. 2014, The Galactic Center: Feeding and Feedback in a Normal Galactic Nucleus, 303, 274
Xu, Y.-D., Narayan, R., Quataert, E., Yuan, F., & Baganoff, F. K. 2006, ApJ, 640, 319
Yuan, F., Quataert, E., & Narayan, R. 2003, ApJ, 598, 301
Yuan, Q., & Wang, Q. D. 2016, MNRAS, 456, 1438
Yusef-Zadeh, F., Bushouse, H., Dowell, C. D., et al. 2006, ApJ, 644, 198
Yusef-Zadeh, F., Wardle, M., Heinke, C., et al. 2008, ApJ, 682, 361-372
Yusef-Zadeh, F., Bushouse, H., Wardle, M., et al. 2009, ApJ, 706, 348
Zhao, J.-H., Young, K. H., Herrnstein, R. M., et al. 2003, ApJ, 586, L29
Zhao, J.-H., Herrnstein, R. M., Bower, G. C., Goss, W. M., & Liu, S. M. 2004, ApJ, 603, L85
Zweibel, E. G., & Yamada, M. 2009, ARA&A, 47, 291